

## Article

# Covalent targeted radioligands potentiate radionuclide therapy

<https://doi.org/10.1038/s41586-024-07461-6>

Received: 19 April 2023

Accepted: 24 April 2024

Published online: 22 May 2024

 Check for updates

Xi-Yang Cui<sup>1,2,7</sup>, Zhu Li<sup>3,7</sup>, Ziren Kong<sup>4,7</sup>, Yu Liu<sup>1</sup>, Hao Meng<sup>2</sup>, Zihao Wen<sup>1</sup>, Changlun Wang<sup>1</sup>, Junyi Chen<sup>1</sup>, Mengxin Xu<sup>1,2</sup>, Yiyuan Li<sup>1</sup>, Jingyue Gao<sup>1</sup>, Wenjia Zhu<sup>5</sup>, Zhixin Hao<sup>5</sup>, Li Huo<sup>5</sup>, Shaoyan Liu<sup>4</sup>, Zhi Yang<sup>3</sup> & Zhibo Liu<sup>1,2,3,6</sup>✉

Targeted radionuclide therapy, in which radiopharmaceuticals deliver potent radionuclides to tumours for localized irradiation, has addressed unmet clinical needs and improved outcomes for patients with cancer<sup>1–4</sup>. A therapeutic radiopharmaceutical must achieve both sustainable tumour targeting and fast clearance from healthy tissue, which remains a major challenge<sup>5,6</sup>. A targeted ligation strategy that selectively fixes the radiopharmaceutical to the target protein in the tumour would be an ideal solution. Here we installed a sulfur (VI) fluoride exchange (SuFEx) chemistry-based linker on radiopharmaceuticals to prevent excessively fast tumour clearance. When the engineered radiopharmaceutical binds to the tumour-specific protein, the system undergoes a binding-to-ligation transition and readily conjugates to the tyrosine residues through the ‘click’ SuFEx reaction. The application of this strategy to a fibroblast activation protein (FAP) inhibitor (FAPI) triggered more than 80% covalent binding to the protein and almost no dissociation for six days. In mice, SuFEx-engineered FAPI showed 257% greater tumour uptake than did the original FAPI, and increased tumour retention by 13-fold. The uptake in healthy tissues was rapidly cleared. In a pilot imaging study, this strategy identified more tumour lesions in patients with cancer than did other methods. SuFEx-engineered FAPI also successfully achieved targeted β- and α-radionuclide therapy, causing nearly complete tumour regression in mice. Another SuFEx-engineered radioligand that targets prostate-specific membrane antigen (PSMA) also showed enhanced therapeutic efficacy. Considering the broad scope of proteins that can potentially be ligated to SuFEx warheads, it might be possible to adapt this strategy to other cancer targets.

Targeted radionuclide therapy (TRT) is a paradigm-shifting therapeutic modality for treating metastatic cancers, which cause the majority of deaths from all cancers<sup>1</sup>. TRT depends on radioligands, which bind to cancer-associated or specific targets with high affinity and deliver potent β-particles or α-particles for localized irradiation<sup>2</sup>. As a new modality for clinical cancer treatment, it features inherent theranostic properties<sup>3</sup>, a ‘crossfire’ effect (eradicating cancer cells that are not necessarily targeted) and independence from the biological pathways of binding targets<sup>4</sup>. US Food and Drug Administration (FDA)-approved radioligands have been routinely used to treat patients with metastatic cancers<sup>7,8</sup>. Notably, the clinical need for TRT is expected to increase, with its emerging clinical benefits in earlier lines of treatment and other indications.

The success of therapeutic radioligands requires excellent tumour targeting, rapid blood clearance and sufficient tumour retention, as the half-lives of most therapeutic radionuclides are three to ten days. However, balancing the blood clearance and tumour retention of a drug is often a challenge<sup>5,6</sup>. The traditional radioligand is often a dual-functional conjugate linking a radionuclide-labelled module with a tumour-targeting ligand. Owing to the reversible interaction of most ligands, the tumour retention of traditional radioligands is often insufficient, which compromises the efficacy of TRT (Fig. 1a, left). A platform technology that irreversibly fixes radioligands to cancer targets in a tumour-selective manner (Fig. 1a, right), if successfully developed, would present an ideal solution to this problem, but has not yet been established.

<sup>1</sup>Beijing National Laboratory for Molecular Sciences, Radiochemistry and Radiation Chemistry Key Laboratory of Fundamental Science, Key Laboratory of Bioorganic Chemistry and Molecular Engineering of Ministry of Education, College of Chemistry and Molecular Engineering, Peking University, Beijing, P. R. China. <sup>2</sup>Changping Laboratory, Beijing, P. R. China. <sup>3</sup>Key Laboratory of Carcinogenesis and Translational Research (Ministry of Education), NMPA Key Laboratory for Research and Evaluation of Radiopharmaceuticals, Department of Nuclear Medicine, Peking University Cancer Hospital and Institute, Beijing, P. R. China. <sup>4</sup>Department of Head and Neck Surgery, National Cancer Center/National Clinical Research Center for Cancer/Cancer Hospital, Chinese Academy of Medical Sciences and Peking Union Medical College, Beijing, P. R. China. <sup>5</sup>Department of Nuclear Medicine, Beijing Key Laboratory of Molecular Targeted Diagnosis and Therapy in Nuclear Medicine and State Key Laboratory of Complex Severe and Rare Diseases, Peking Union Medical College Hospital, Chinese Academy of Medical Sciences and Peking Union Medical College, Beijing, P. R. China. <sup>6</sup>Peking University-Tsinghua University Center for Life Sciences, Peking University, Beijing, P. R. China. <sup>7</sup>These authors contributed equally: Xi-Yang Cui, Zhu Li, Ziren Kong. ✉e-mail: zbliu@pku.edu.cn

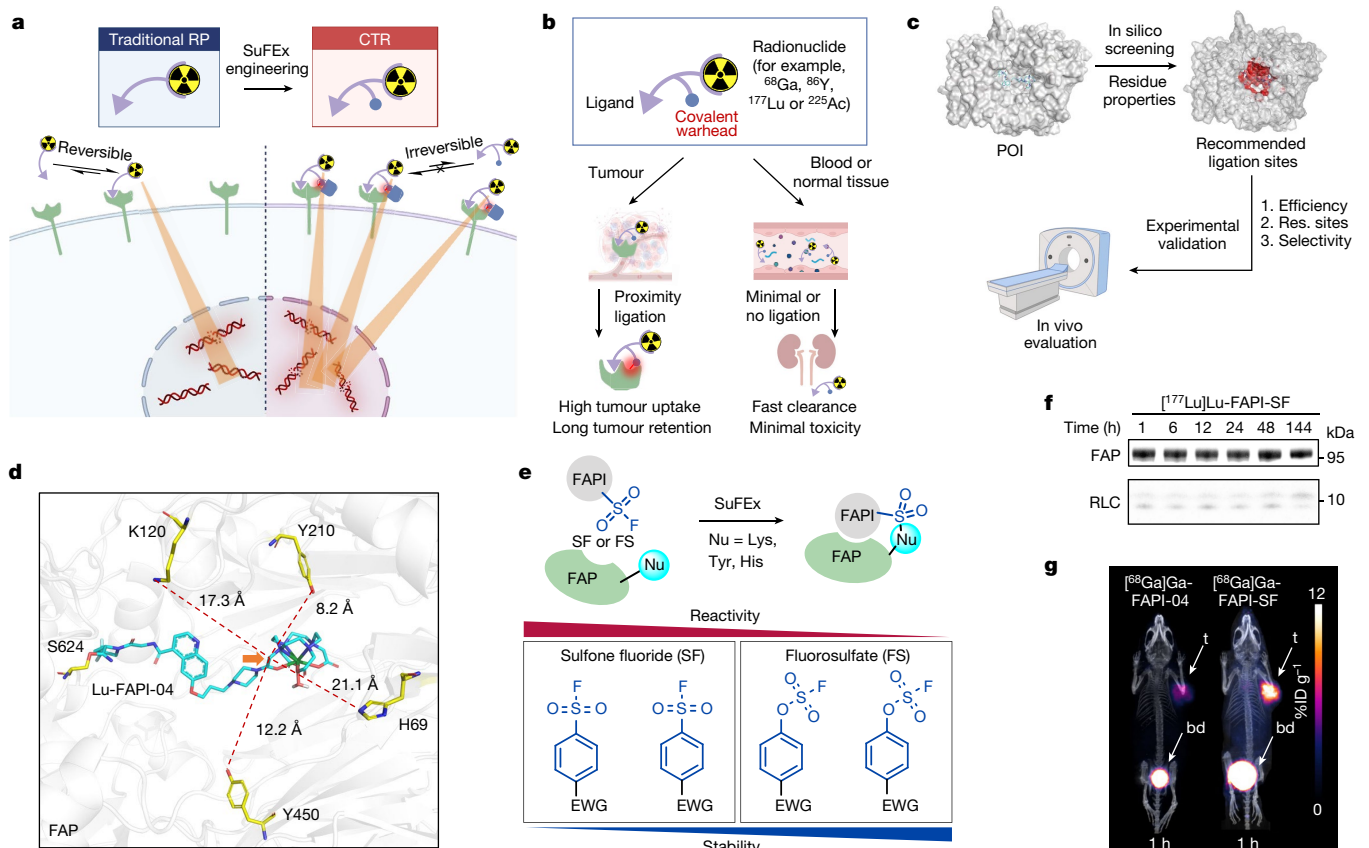


**Fig. 1 | Development of a CTR by SuFEx engineering and successful proof of concept in tumour-bearing mice.** **a**, Schematic representation of the potential benefits of CTRs over traditional radiopharmaceuticals (RPs) for TRT. **b**, Ideal working model of a CTR. **c**, Overall procedure for CTR development. All of the residues (res.) in the pocket of a protein of interest (POI) were computationally screened according to their properties, including solvent accessibility and distance to the modification starting point. The recommended residue sites for ligation were then subjected to structure-based drug design and experimental validation including *in vivo* PET/CT evaluation. **d**, Molecular docking of Lu-FAPI-04 (cyan) against FAP (grey; Protein Data Bank (PDB): 1Z68) showing the selected possible ligation residues. The carbon selected for SuFEx engineering in this work is indicated with an orange arrow.

**e**, Scheme of proximity-enabled SuFEx ligation on FAP. The SuFEx covalent warheads screened in this work and the relationships between structure, activity and stability are summarized. EDG, electron-donating group; EWG, electron-withdrawing group; Nu, nucleophile at side chain. **f**, Analysis of FAPI-SF binding to FAP *in vitro*. Purified human FAP (3  $\mu$ M) in PBS buffer (pH 7.4) was incubated with [ $^{177}$ Lu]Lu-FAPI-SF (0.15  $\mu$ M) at 37 °C. The upper bands indicate that FAPI-SF is irreversibly bound to FAP. **g**, PET/CT images of the same HT-1080-FAP tumour-bearing mouse intravenously injected with [ $^{68}$ Ga]Ga-FAPI-04 and [ $^{68}$ Ga]Ga-FAPI-SF, respectively, at a 12-h interval. bd, bladder; ID, injected dose; t, tumour. Data are representative of three independent experiments (**f**). RLC, radionuclide–ligand conjugate. The illustrations in **a–c** were created with BioRender.

The covalent engineering of drug molecules has emerged as a key strategy to prolong the duration of action<sup>9,10</sup>. We surmised that modern covalent engineering strategies might be able to enhance the tumour uptake and retention of radioligands, but that they must avoid uncontrollable ligation reactivity during circulation or in healthy tissues. Therefore, we aimed to develop a covalent targeted radioligand (CTR), and the *in vivo* working model for this is shown in Fig. 1b. It is a trifunctional conjugate generated by attaching a radioligand molecule to a suitable covalent warhead at the right position and orientation to achieve ligation without loss of affinity. Furthermore, when CTRs reach the tumour, they first noncovalently bind to the target and subsequently undergo irreversible covalent binding enabled by proximity, minimizing the clearance rate. Other free CTRs that do not bind to the target would undergo fast excretion without off-target ligation owing to the relative bio-orthogonality of the specific warheads<sup>11</sup>, thus limiting the risk of systemic toxicity.

## CTRs increase the tumour uptake of radioligands

As a proof of concept, we chose fibroblast activation protein (FAP), a type II transmembrane serine peptidase, as the target for the development of a CTR. We prioritized this target because, first, FAP

is a pan-cancer target with high tumour-specific expression<sup>12</sup>; and, second, FAPI-04, a DOTA-conjugated FAP inhibitor (FAPI)<sup>13</sup> that has a high tumour-to-background ratio (TBR) and rapid renal clearance, has been successfully used in diagnosing more than 28 types of cancers<sup>14</sup>. However, no FAPIs thus far have achieved conclusively satisfactory clinical therapeutic results owing to their low tumour uptake and overly rapid clearance from tumours<sup>15</sup>. The general workflow for CTR design is shown in Fig. 1c. We first used GOLD software with reference to the Lu-DOTA crystal structure (Cambridge Crystallographic Data Centre (CCDC) identifier: NOJYIU) to conduct precise docking of Lu-FAPI-04 (ref. 16) (Fig. 1d). The interactions of Lu-FAPI-04's targeting module with key residues (Supplementary Fig. 6), for example, S624, Y656 and R123, are analogous to those of a DPP-4 inhibitor<sup>17</sup>. According to the synthetic accessibility of FAPI-04 (refs. 18,19), the carbon indicated by the orange arrow in Fig 1d was selected as the starting point for the modification. We identified the solvent-accessible residues in the binding pocket and then evaluated their key parameters—including accessible surface area, residue per cent exposure, pKa value, charge, distance (to the modification starting point) and location—to identify nearby residues as ‘grips’ for ligation (Supplementary Table 2). The microenvironment in the FAP active site, which contains the highly nucleophilic Y450 and neighbouring Y210, directed our attention to

sulfur (VI) fluoride exchange (SuFEx) latent warheads, which exhibit reactivity with a wide range of amino acids, including tyrosine<sup>20</sup>. Their reported proximity-enabled reactivity endows them with high stability and bio-orthogonality before they reach their target, which enables them to be used on small-molecule inhibitors<sup>21,22</sup>, proteins<sup>23</sup> and other biomolecules<sup>24,25</sup>. Although none of them has been evaluated for clinical use until this work, several latent covalent warheads, including aryl-sulfone fluoride (SF) and aryl fluorosulfate (FS), have been added to the covalent engineering arsenal.

With a SuFEx warhead installed, FAP-targeted CTR (CTR-FAPI) can undergo a proximity-enabled reaction in the binding pocket (Fig. 1e). After pretesting the structure–activity relationships of the SF and FS groups, FAPI-SF (**1**) with SF, which has an electron-donating methylene group, was synthesized and radiolabelled (Extended Data Fig. 1), because SF is more reactive and was considered to be likely to provide a positive ligation result. By autoradioluminography, <sup>177</sup>Lu-labelled FAPI-SF exhibited fast and irreversible covalent binding after incubation with FAP in vitro (Fig. 1f). Next, [<sup>68</sup>Ga]Ga-FAPI-04 as a control and [<sup>68</sup>Ga]Ga-FAPI-SF were tested in the same HT-1080-FAP tumour-bearing mouse. Positron emission tomography and computed tomography (PET/CT) imaging clearly revealed that [<sup>68</sup>Ga]Ga-FAPI-SF had markedly greater tumour uptake than did [<sup>68</sup>Ga]Ga-FAPI-04 (Fig. 1g). Its clearance is rapid and occurs mainly through the renal system, with almost negligible accumulation in other major organs. The maximum standard uptake value (SUV) of [<sup>68</sup>Ga]Ga-FAPI-SF in the tumour increased to  $10.5 \pm 1.3\%$  injected dose per gram (%ID g<sup>-1</sup>) at 1 h after injection ( $n = 4$ ; Supplementary Fig. 7), which was double that of [<sup>68</sup>Ga]Ga-FAPI-04. This first attempt suggested that the covalent radioligand strategy might be promising. However, the stability assay showed that more than 50% of FAPI-SF underwent hydrolysis in 24 h in phosphate-buffered saline (PBS; pH 7.4, 37 °C; Extended Data Fig. 2e), which suggests that the SF warhead is overly reactive, leading to undesired off-target ligation.

### CTR-FAPIs bind irreversibly to FAP

We hypothesized that alternative FS warheads with lower reactivity might provide greater *in vivo* stability and better tumour targeting<sup>26</sup>. Two new CTR-FAPIs with electron-withdrawing amide-substituted FS warheads—FAPI-pFS and FAPI-mFS—were synthesized<sup>27</sup> and radiolabelled with <sup>68</sup>Ga or <sup>177</sup>Lu (Extended Data Fig. 1). As hoped, the stabilities of FAPI-pFS and FAPI-mFS were greater than 95% after incubation under physiological conditions (PBS pH 7.4, 37 °C) for 72 h (Extended Data Fig. 1c). Before proceeding to *in vivo* study, we investigated whether FAPI-04, FAPI-pFS and FAPI-mFS bound irreversibly to FAP (Fig. 2a, top) and, if so, which amino acid residues of FAP were ligated to the CTR-FAPI molecules (Fig. 2a, bottom). The SDS–PAGE–autoradioluminography tandem assay showed that FAPI-pFS and FAPI-mFS exhibit efficient (more than 90% ligation yields) and robust (at least 144 h) irreversible covalent binding with FAP (Fig. 2b). By contrast, although FAPI-04 may form a reversible covalent bond with FAP, the complex then completely dissociates owing to the thermo-instability of the imidate<sup>28</sup>, which has a half-life of only approximately 9.6 h *in vitro* even without cellular metabolism (Supplementary Fig. 8b). A binding model of CTR-FAPI was rationalized on the basis of the acid treatment experiment: most of the FAPI-04 rapidly dissociated from FAP if the imidate bond was broken at low pH, whereas the binding of FAPI-mFS was not affected by the same treatment (Extended Data Fig. 3a,b). The rate constant of this irreversible SuFEx reaction was calculated, on the basis of the model, to be approximately 0.25 M<sup>-1</sup> min<sup>-1</sup> (Extended Data Fig. 3c,e), which suggests that the existing suboptimal SuFEx warheads could be further improved—for example, by using activity-based protein profiling methods<sup>29</sup>—to obtain more specific and efficient targeted covalent linkages.

We purified <sup>nat</sup>Lu-FAPI-pFS (in which superscript ‘nat’ means natural or non-radioactive) or <sup>nat</sup>Lu-FAPI-mFS ligated protein complexes

by SDS–PAGE for trypsin cleavage and collected the corresponding tandem mass spectra. The representative modification residues are shown in Fig. 2c and Supplementary Figs. 9 and 10. As expected, Y210 and Y450 were both modified by <sup>nat</sup>Lu-FAPI-pFS or <sup>nat</sup>Lu-FAPI-mFS after the SuFEx reaction, resulting in the loss of one molecule of HF (*m/z* –20). Subsequent molecular dynamics (MD) simulations of bonded Lu-FAPI-pFS-Y<sup>210</sup>-FAP and Lu-FAPI-mFS-Y<sup>450</sup>-FAP complexes further demonstrated the stability of these ligations (Fig. 2d and Supplementary Figs. 11–14). We also performed surface plasmon resonance (SPR) in single-cycle mode to investigate the molecule–target interaction kinetics<sup>30</sup> (Extended Data Fig. 4a). On the basis of the key constants presented in Extended Data Fig. 4b,c, FAPI-pFS and FAPI-mFS bind to FAP 43 and 15 times faster, respectively, than they do to FAPI-04. FAPI-pFS and FAPI-mFS also dissociate from FAP at a much lower rate than they do from the reversibly bound FAPI-04, whereas the FS-hydrolysed control FAPI-mHS exhibits a dissociation rate similar to that of FAPI-04, suggesting that the induction of FS results in irreversible binding to FAP.

Covalent binding may efficiently increase the cellular uptake and retention of radioligands. Incubation of radiolabelled FAPI-04 or CTR-FAPIs with HT-1080-FAP cells showed that the cell accumulation of [<sup>68</sup>Ga]Ga-CTR-FAPIs ( $50.0 \pm 7.3\%$  ID, FAPI-pFS;  $39.5 \pm 2.3\%$  ID, FAPI-mFS) was rapid and almost fourfold greater than that of [<sup>68</sup>Ga]Ga-FAPI-04 ( $7.8 \pm 0.5\%$  ID) in the first 30 min (Fig. 2e, left). Notably, the cell uptake of CTR-FAPIs continued to increase at four hours after incubation, whereas the uptake of FAPI-04 started to decrease. After incubation, we also performed SDS–PAGE autoradiography analysis of the total proteins extracted from the cells. As shown in Fig. 2e (right), FAPI-pFS and FAPI-mFS efficiently and robustly formed covalent bonds to FAP on cells. The ligation ratios were slightly lower than the cell uptake ratios, owing probably to the subtraction of nonspecific binding. The cell retention of FAPIs was assayed by an efflux experiment (Fig. 2f). The half-lives of FAPI-pFS and FAPI-mFS are approximately 33 h and 39 h, respectively, which are up to 13.9 times longer than that of FAPI-04 (2.8 h).

We also synthesized the fluorogenic probe FAPI-AF488-mFS (Extended Data Fig. 2a) to visualize cell uptake and efflux (Extended Data Fig. 4d–f). The control probe FAPI-AF488-mHS was prepared by hydrolysis of the FS warhead. Compared with FAPI-AF488-mFS, the noncovalent FAPI-AF488-mHS lacked sustained uptake (Extended Data Fig. 4d). The half-life was approximately 40 h for FAPI-AF488-mFS and less than 2 h for FAPI-AF488-mHS, as shown by the decrease in fluorescence intensity (Extended Data Fig. 4f). These data suggest that SuFEx engineering can increase the cellular uptake and retention of FAPI and its derivatives. However, whether CTR-FAPIs can efficiently anchor FAP in tumour-bearing mice with dynamic blood circulation<sup>31</sup> (Extended Data Fig. 4g) by leveraging the tumour uptake of rapidly cleared FAP-targeted radioligands, such as FAPI-04, is still unclear.

### CTR-FAPI PET shows better imaging contrast

A general concern about covalent drugs is their potential for off-target binding. We first tested the binding affinity of SuFEx-engineered FAPIs for FAP homologous prolyl oligopeptidases, mainly DPP-4 and prolyl endopeptidase (PREP)<sup>13</sup>, and found that the FAP selectivities were as high as those for FAPI-04 (Extended Data Figs. 2d and 5a). In addition, because of their highly hydrophilic and multicharged chelators (for example, DOTA), most radioligands have limited passive permeability to the cell membrane; thus, off-target ligation to intracellular targets might not be a concern. We also performed SDS–PAGE autoradiography analysis of samples from CTR-FAPIs incubated in human serum (Extended Data Fig. 5b,d) or from mouse blood after the injection of CTR-FAPIs (Extended Data Fig. 5c). Notably, we found that both FAPI-SF and FAPI-pFS can undergo undesired ligation with albumin, which is the most abundant protein in the blood (up to around 50 g l<sup>-1</sup>). However,

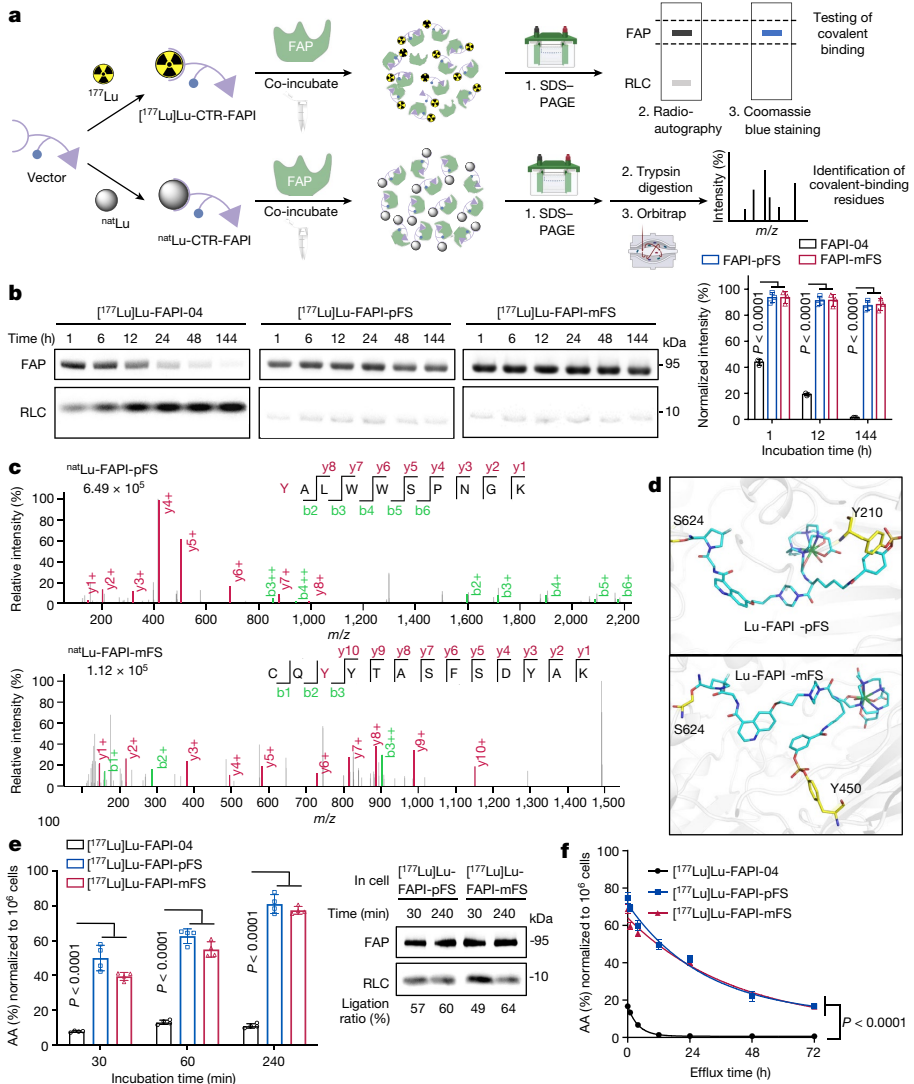


**Fig. 2 | CTR-FAPIs irreversibly bind to FAP through covalent ligation to the tyrosine residues, leading to higher uptake and longer retention in cancer cells.** **a**, Workflow for investigating the covalent mechanism. Top, SDS-PAGE and autoradioluminography tandem assay to test covalent binding. Bottom, tandem mass spectrometry assay to identify the residues of covalent binding. **b**, Analysis of FAPI-04, FAPI-pFS and FAPI-mFS binding to FAP in vitro. Purified human FAP (3 μM) in PBS buffer (pH 6.5) was incubated with <sup>177</sup>Lu-labelled conjugates (0.15 μM) at 37 °C. The experiment was repeated three times and representative results are shown. **c**, Tandem mass spectrometry spectra of the purified CTR-FAPI–FAP protein ligation complex show that <sup>nat</sup>Lu-FAPI-pFS reacts mainly with Y210 (top), whereas <sup>nat</sup>Lu-FAPI-mFS reacts mainly with Y450 (bottom). **d**, Representative snapshots of the FAPI-pFS–FAP complex (top) and the FAPI-mFS–FAP complex (bottom) from the stable trajectories by MD simulations. **e**, Left, cell uptake assay of the <sup>68</sup>Ga-labelled FAPI and CTR-FAPIs in HT-1080-FAP cells after incubation for 0.5–4 h ( $n = 4$ ). Data are per cent added activity (AA) normalized to  $10^6$  cells. Right, the ligation of FAP extracted from cells with <sup>68</sup>Ga-Ga-CTR-FAPIs was observed and quantified. **f**, Cell retention assay evaluating the efflux kinetics of <sup>177</sup>Lu-labelled FAPI and CTR-FAPIs ( $n = 4$ ). HT-1080-FAP cells were incubated with agents for 1 h, followed by incubation with compound-free medium for 1–72 h. Data are mean  $\pm$  s.d. (b,e,f). One-way ANOVA followed by Tukey's multiple comparison test (b,e) and two-tailed unpaired Student's *t*-test (f at 72 h). The illustrations in a were created with BioRender.

FAPI-mFS showed almost no ligation to human serum protein within hours. In the urine stability assay, no other radioactive species were detected, but only <sup>177</sup>Lu-Lu-FAPI-mFS itself was detected at 30 min after administration, when most of the FAPI-mFS was excreted (Extended Data Fig. 5e). The above results suggest that the SuFEx-engineered warhead, especially mFS, might not cause off-target covalent binding in healthy tissues.

We then tested whether FS-conjugated FAPIs could achieve extra tumour uptake and a clearer background in tumour-bearing mice. Head-to-head PET/CT imaging of <sup>[68]Ga</sup>Ga-FAPI-04 and <sup>[68]Ga</sup>Ga-FAPI-pFS (or <sup>[68]Ga</sup>Ga-FAPI-mFS) was subsequently performed in the same tumour-bearing mice (an assay validation is shown in Supplementary Fig. 15). As shown in Fig. 3a, <sup>[68]Ga</sup>Ga-FAPI-pFS and

<sup>[68]Ga</sup>Ga-FAPI-mFS exhibited notably greater tumour uptake than did FAPI-04 ( $n = 4$ ) at one hour after injection, with the maximum SUV ( $SUV_{max}$ ) increasing by 92% and 257%, respectively (Fig. 3b). As desired, the clearance of <sup>[68]Ga</sup>Ga-FAPI-pFS and <sup>[68]Ga</sup>Ga-FAPI-mFS is rapid and occurs mainly through the renal system. The uptake in other major organs, which can cause toxicity, was almost negligible in subsequent treatment assays. We also determined the ex vivo biodistribution of <sup>[68]Ga</sup>Ga-FAPI-SF, <sup>[68]Ga</sup>Ga-FAPI-pFS and <sup>[68]Ga</sup>Ga-FAPI-mFS at five hours after injection ( $n = 7$ ; Fig. 3d). <sup>[68]Ga</sup>Ga-FAPI-mFS had significantly greater tumour uptake ( $12.1 \pm 1.2\%ID g^{-1}$ ) than did <sup>[68]Ga</sup>Ga-FAPI-pFS ( $8.2 \pm 1.7\%ID g^{-1}$ ) and <sup>[68]Ga</sup>Ga-FAPI-SF ( $8.9 \pm 1.7\%ID g^{-1}$ ) but had overall lower uptake in major organs. These results suggested that FAPI-mFS should be used for subsequent TRT.

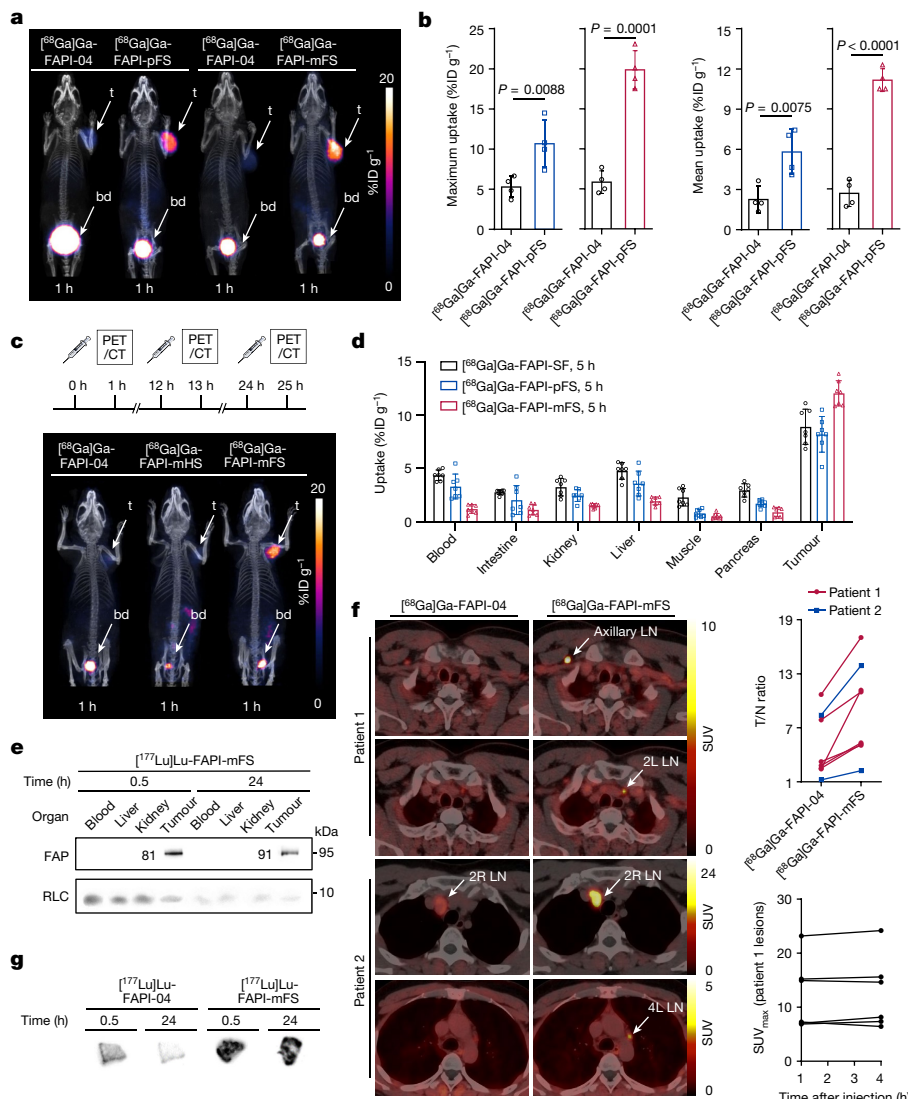


**Fig. 3 | CTR-FAPIs improve tumour uptake in tumour-bearing mice and precisely detect lesions in patients with cancer.** **a**, PET/CT imaging assays of [<sup>68</sup>Ga]Ga-FAPI-pFS or [<sup>68</sup>Ga]Ga-FAPI-mFS and [<sup>68</sup>Ga]Ga-FAPI-04 in the same HT-1080-FAP tumour-bearing mice. **b**, Maximum (left) and mean (right) tumour uptakes of [<sup>68</sup>Ga]Ga-FAPI-04, [<sup>68</sup>Ga]Ga-FAPI-pFS and [<sup>68</sup>Ga]Ga-FAPI-mFS in tumours at one hour after injection ( $n = 4$  mice per group). **c**, Sequential PET/CT imaging of [<sup>68</sup>Ga]Ga-FAPI-04, [<sup>68</sup>Ga]Ga-FAPI-mFS and its FS-warhead-hydrolysed control ([<sup>68</sup>Ga]Ga-FAPI-mHS) in the same tumour-bearing mice, highlighting the key effect of the covalent warhead. **d**, Biodistribution study of [<sup>68</sup>Ga]Ga-FAPI-SF, [<sup>68</sup>Ga]Ga-FAPI-pFS and [<sup>68</sup>Ga]Ga-FAPI-mFS in HT-1080-FAP tumour-bearing mice, suggesting that FAPI-mFS has the highest tumour uptake and the lowest background ( $n = 7$  mice per group,  $P$  values are summarized in Supplementary Table 14). **e**, [<sup>177</sup>Lu]Lu-FAPI-mFS ligated selectively to FAP extracted from mouse tumours. Ligation ratios (%) are presented beside the corresponding bands. **f**, Pilot PET/CT study of [<sup>68</sup>Ga]Ga-FAPI-mFS compared with [<sup>68</sup>Ga]Ga-FAPI-04 in patients with mediastinal metastatic MTC. Top right, tumour-to-normal (T/N) ratios are enhanced in patients treated with [<sup>68</sup>Ga]Ga-FAPI-mFS compared with those treated with [<sup>68</sup>Ga]Ga-FAPI-04 ( $n = 8$  lesions from 2 patients). Bottom right, the PET/CT imaging for patient 1 four hours after injection with [<sup>68</sup>Ga]Ga-FAPI-mFS shows that the tumour uptake is maintained. **g**, PET/CT imaging of patient 1 four hours after injection with [<sup>177</sup>Lu]Lu-FAPI-mFS shows minimal dissociation in FAP-positive tumour tissues from a patient with MTC. The fresh adjacent tissues from the same lesion were immersed in tissue storage solution containing [<sup>177</sup>Lu]Lu-FAPI-04 or [<sup>177</sup>Lu]Lu-FAPI-mFS for 30 min, before a 4–24-h incubation in the blank solution. Representative autoradioluminographic images of the tissues are shown. Data are mean  $\pm$  s.d. (**b**, **d**). Two-tailed paired Student's *t*-test (**b**) and one-way ANOVA followed by Tukey's multiple comparison test (**d**). Data are representative of two (**e**) or three (**g**) independent experiments.

corresponding bands. **f**, Pilot PET/CT study of [<sup>68</sup>Ga]Ga-FAPI-mFS compared with [<sup>68</sup>Ga]Ga-FAPI-04 in patients with mediastinal metastatic MTC. Top right, tumour-to-normal (T/N) ratios are enhanced in patients treated with [<sup>68</sup>Ga]Ga-FAPI-mFS compared with those treated with [<sup>68</sup>Ga]Ga-FAPI-04 ( $n = 8$  lesions from 2 patients). Bottom right, the PET/CT imaging for patient 1 four hours after injection with [<sup>68</sup>Ga]Ga-FAPI-mFS shows that the tumour uptake is maintained. **g**, PET/CT imaging of patient 1 four hours after injection with [<sup>177</sup>Lu]Lu-FAPI-mFS shows minimal dissociation in FAP-positive tumour tissues from a patient with MTC. The fresh adjacent tissues from the same lesion were immersed in tissue storage solution containing [<sup>177</sup>Lu]Lu-FAPI-04 or [<sup>177</sup>Lu]Lu-FAPI-mFS for 30 min, before a 4–24-h incubation in the blank solution. Representative autoradioluminographic images of the tissues are shown. Data are mean  $\pm$  s.d. (**b**, **d**). Two-tailed paired Student's *t*-test (**b**) and one-way ANOVA followed by Tukey's multiple comparison test (**d**). Data are representative of two (**e**) or three (**g**) independent experiments.

We also examined whether the SuFEx warhead made a major contribution to the tumour targeting of FAPI-mFS. As a control, FAPI-mHS was prepared by hydrolysing FS to hydrogen sulfate. One hour after injection, PET/CT imaging studies were performed in the same tumour-bearing mouse at 12-h intervals with sequential injections of [<sup>68</sup>Ga]Ga-FAPI-04, [<sup>68</sup>Ga]Ga-FAPI-mHS and [<sup>68</sup>Ga]Ga-FAPI-mFS (Fig. 3c and Supplementary Fig. 16). As expected, [<sup>68</sup>Ga]Ga-FAPI-mHS ( $2.8 \pm 0.6\%ID\text{ g}^{-1}$ ;  $n = 4$ ) showed minimal tumour uptake, similar to [<sup>68</sup>Ga]Ga-FAPI-04 ( $2.6 \pm 0.5\%ID\text{ g}^{-1}$ ;  $n = 4$ ), which was notably lower than that of [<sup>68</sup>Ga]Ga-FAPI-mFS ( $11.3 \pm 1.4\%ID\text{ g}^{-1}$ ;  $n = 4$ ), suggesting that the

covalent-binding warhead is the key to increasing tumour uptake. In addition, marked covalent binding of FAPI-mFS to FAP in the tumour was observed after injecting [<sup>177</sup>Lu]Lu-FAPI-mFS into tumour-bearing mice (Fig. 3e).

Encouraged by these promising preclinical data, we performed an investigator-initiated trial of [<sup>68</sup>Ga]Ga-FAPI-mFS in patients with cancer. Medullary thyroid carcinoma (MTC) is a type of neuroendocrine tumour that necessitates complete surgical resection as a curative option. However, the use of common radiotracers for imaging neuroendocrine tumours is insufficient to map the extent of the disease<sup>32</sup>.

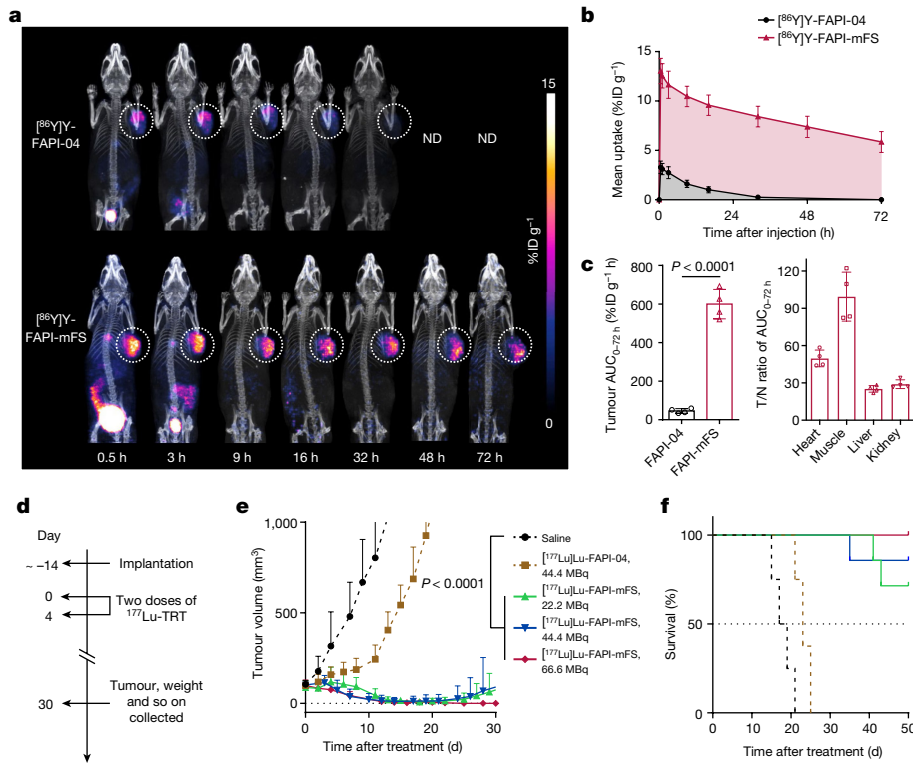


**Fig. 4 | SuFEx-engineered FAPI improves the retention of radionuclides in tumours and causes almost-complete tumour regression.** **a**, Dynamic PET/CT imaging showing that [<sup>86</sup>Y]Y-FAPI-mFS has a notably longer tumour retention than does [<sup>86</sup>Y]Y-FAPI-04 in HT-1080-FAP tumour-bearing mice. ND, not determined. **b**, Time–radioactivity curves of [<sup>86</sup>Y]Y-FAPI-mFS and [<sup>86</sup>Y]Y-FAPI-04 in tumours ( $n = 4$  mice per group). **c**, Integrated AUC (left; in %ID g<sup>-1</sup> h) between [<sup>86</sup>Y]Y-FAPI-mFS and [<sup>86</sup>Y]Y-FAPI-04 and T/N ratios (right)

( $n = 4$  mice per group). **d–f**, NU/NU mice were implanted subcutaneously with HT-1080-FAP cells, followed by intravenous injection of saline, [<sup>177</sup>Lu]Lu-FAPI-04 or [<sup>177</sup>Lu]Lu-FAPI-mFS. **d**, Treatment scheme. **e**, Average tumour volumes of each group.  $n = 7$  mice for each [<sup>177</sup>Lu]Lu-FAPI-mFS group;  $n = 8$  mice for the saline and the [<sup>177</sup>Lu]Lu-FAPI-04 groups. **f**, Kaplan–Meier survival curve 50 days after treatment. Data are mean  $\pm$  s.d. (**b,c,e**). Two-tailed unpaired *t*-test (**c** and **e** on day 15).

The initial study of FAPI-04 reported low uptake in MTC lesions, demonstrating the difficulty of FAP imaging in patients with MTC (ref. 14). In two representative patients with MTC with mediastinal lymph node (LN) metastasis, [<sup>68</sup>Ga]Ga-FAPI-mFS identified more suspicious lesions ( $n = 8$ ) than did [<sup>68</sup>Ga]Ga-FAPI-04 ( $n = 4$ ), according to visual evaluation (Fig. 3f and Extended Data Fig. 5g), owing to its significantly greater tumour uptake and tumour-to-normal (T/N) ratio (SUV<sub>max</sub>  $12.68 \pm 7.63$  versus  $7.90 \pm 5.69$ ; T/N ratio  $8.86 \pm 5.16$  versus  $4.90 \pm 3.53$ , 1 h after administration). The tumour uptake remained high (SUV<sub>max</sub>  $12.42 \pm 6.57$ ,  $n = 6$ , 1 h after injection; SUV<sub>max</sub>  $12.24 \pm 6.67$ ,  $n = 6$ , 4 h after injection) for patient 1, who underwent PET/CT imaging four hours after injection, whereas the uptake decreased for major organs (Extended Data Fig. 5h). Notably, we also used radio-high-performance liquid chromatography (radio-HPLC) to detect radioactive species in the urine sample from this patient collected 30 min after injection, and the peak had the same retention time as that of the original [<sup>68</sup>Ga]Ga-FAPI-mFS, indicating greater than 99% stability (Extended Data Fig. 5f). After mediastinal LN dissection, all resectable [<sup>68</sup>Ga]Ga-FAPI-mFS-avid mediastinal lesions were found by immunohistochemistry analysis to be metastatic MTC with high levels of FAP expression ( $n = 7$ ; Supplementary Fig. 17), and the three regional LNs would have been missed during surgery without [<sup>68</sup>Ga]Ga-FAPI-mFS. We also compared the efflux behaviour of [<sup>177</sup>Lu]Lu-FAPI-04 and [<sup>177</sup>Lu]Lu-FAPI-mFS in the resected fresh lesion (2R LN) from patient 1 by autoradioluminography. The results showed high and persistent tumour binding of [<sup>177</sup>Lu]Lu-FAPI-mFS, whereas [<sup>177</sup>Lu]Lu-FAPI-04 bound moderately and exhibited significant dissociation after 24 h of incubation in blank tissue storage solution (Fig. 3g and Supplementary Fig. 18).

## CTR potentiates FAP-TRT by improved retention

After diagnosing cancer using <sup>68</sup>Ga, which has a short half-life, we studied the long-term pharmacokinetics of FAPI-mFS for therapy<sup>33</sup>. In tumour-bearing mice, [<sup>86</sup>Y]Y-FAPI-mFS accumulated more rapidly in the tumour, with greater uptake, compared with [<sup>86</sup>Y]Y-FAPI-04, and almost no clearance was observed until 72 h (Fig. 4a). The tumour radioactivity–time curves of [<sup>86</sup>Y]Y-FAPI-04 and [<sup>86</sup>Y]Y-FAPI-mFS (Fig. 4b) show that the integrated area under the curve (AUC) of [<sup>86</sup>Y]Y-FAPI-mFS is up to 13 times greater than that of [<sup>86</sup>Y]Y-FAPI-04 (Fig. 4c, left). The T/N AUC ratios of [<sup>86</sup>Y]Y-FAPI-mFS were  $49.75 \pm 7.70$ ,  $99.46 \pm 19.71$ ,  $25.24 \pm 2.68$  and  $29.02 \pm 3.52$  in the heart, muscle, liver and kidney, respectively ( $n = 4$ ; Fig. 4c, right and Supplementary Fig. 19). The above results also corroborate the biodistribution of [<sup>177</sup>Lu]Lu-FAPI-04 and [<sup>177</sup>Lu]Lu-FAPI-mFS in tumour-bearing mice (Supplementary Figs. 20–22), providing evidence of the excellent targeting and retention of FAPI-mFS in tumours.

On the basis of the biodistribution, the effective dose of [<sup>177</sup>Lu]Lu-FAPI-mFS for the treatment of HT-1080-FAP tumours was calculated by OLINDA software to be 890 mGy MBq<sup>-1</sup> (Supplementary Table 3); accordingly, we used a high dose of up to 66.6 MBq, which is comparable with those in a previous report<sup>34</sup>, and could be delivered to tumours with a standard high radiation dose (60 Gy) (Fig. 4d). As expected, in saline-treated control mice, the volume of the HT-1080-FAP tumours increased by more than tenfold at 15 days (Fig. 4e,f and Extended Data Fig. 6a). Notably, after treatment with two rounds of 22.2 MBq of [<sup>177</sup>Lu]Lu-FAPI-mFS, most of the tumours stopped growing in the first few days, and subsequently, substantial tumour shrinkage was observed. Two rounds of [<sup>177</sup>Lu]Lu-FAPI-mFS treatment (33.3 MBq)

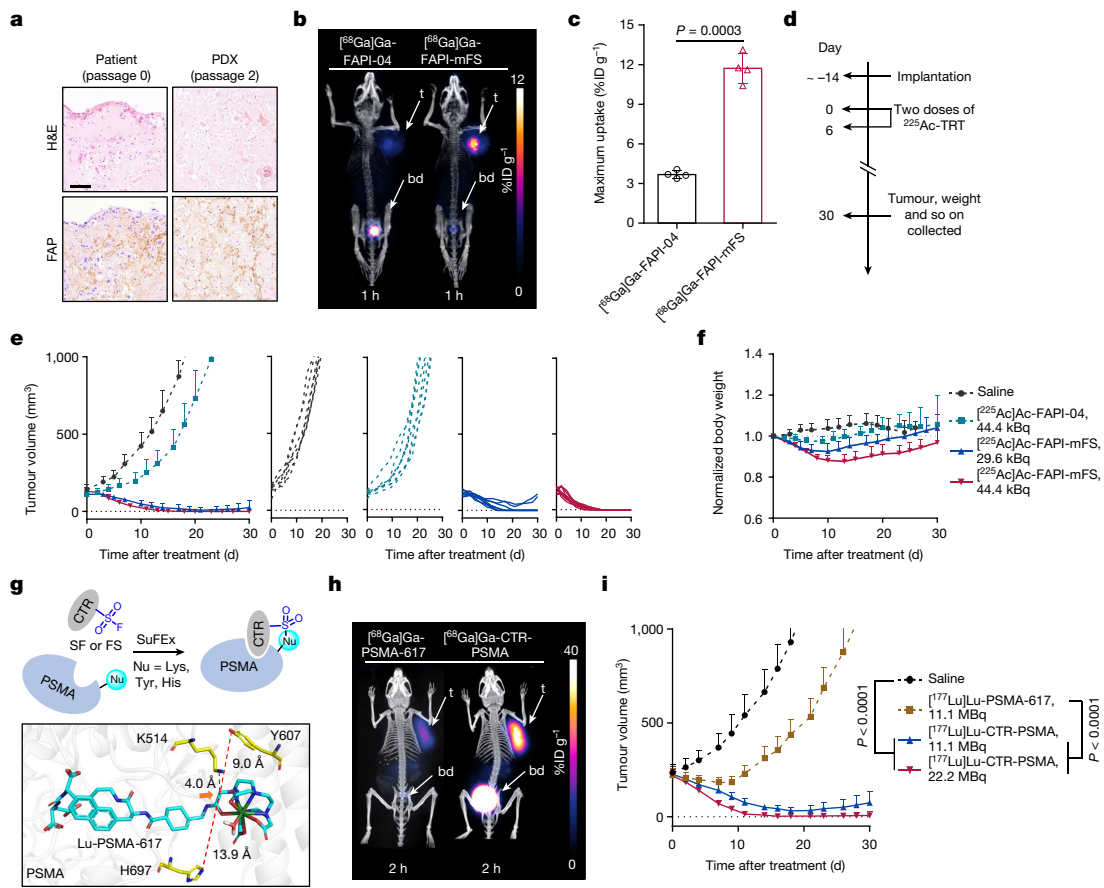


**Fig. 5 | Performance of SuFEx-engineered FAPI in targeted- $\alpha$ -therapy in an HT-1080-FAP cell-line-derived xenograft model and an SDC-PDX model.**

**a**, Immunohistochemistry analysis of tumour samples from the patient and the SDC-PDX model. Scale bar, 100  $\mu$ m. Data are representative of two independent experiments. **b**, PET/CT imaging of [ $^{68}$ Ga]Ga-FAPI-mFS and [ $^{68}$ Ga]Ga-FAPI-04 in the same PDX mouse at a 12-h interval. **c**, Maximum uptake of [ $^{68}$ Ga]Ga-FAPI-04 and [ $^{68}$ Ga]Ga-FAPI-mFS in tumours one hour after injection ( $n = 4$  mice). **d–f**, Treatment assay with PDX NOD SCID mice that were intravenously injected with saline, [ $^{225}$ Ac]Ac-FAPI-04 or [ $^{225}$ Ac]Ac-FAPI-mFS. **d**, Treatment scheme.  $n = 7$  mice for saline,  $n = 8$  mice for [ $^{225}$ Ac]Ac-FAPI-04 and [ $^{225}$ Ac]Ac-FAPI-mFS. **e**, Tumour volume curves for the group or for an individual mouse. [ $^{225}$ Ac]Ac-FAPI-mFS showed statistically significant differences compared with saline

and [ $^{225}$ Ac]Ac-FAPI-04 ( $P < 0.0001$ ). **f**, Normalized average body weights.

**g**, Molecular docking of Lu-PSMA-617 (cyan) against PSMA protein (grey; PDB: 5OST) showing the selected possible ligation residues. The carbon selected for SuFEx engineering in this work is indicated with an orange arrow. Analysis of [ $^{177}$ Lu]Lu-CTR-PSMA binding to the target protein in vitro. **h**, PET/CT images of the same LNCaP tumour-bearing mouse intravenously injected with [ $^{68}$ Ga]Ga-PSMA-617 and [ $^{68}$ Ga]Ga-CTR-PSMA at 24-h intervals. **i**, NOD SCID mice were implanted subcutaneously with LNCaP cells, followed by intravenous injection of saline, [ $^{177}$ Lu]Lu-PSMA-617 or [ $^{177}$ Lu]Lu-CTR-PSMA.  $n = 8$  mice per group. Average tumour volume curves for each group. Data are mean  $\pm$  s.d. (**c,e,f,i**). Two-tailed paired Student's *t*-test (**c**) and two-tailed unpaired *t*-test analysis (**e,i**, both on day 15).

achieved complete tumour suppression in all mice (7/7), and no recurrence was observed for up to 50 days. By contrast, mice treated for two cycles with [ $^{177}$ Lu]Lu-FAPI-04 (22.2 MBq) still exhibited aggressive tumour growth (Extended Data Fig. 6c). Photography of the tumour confirmed the antitumour effect of [ $^{177}$ Lu]Lu-FAPI-mFS treatment in another repeated trial (Extended Data Fig. 6d). Although treatment with [ $^{177}$ Lu]Lu-FAPI-mFS induced strong tumour regression, the treated mice showed recoverable weight loss (Supplementary Fig. 24a). These findings suggest that the therapeutic CTR-FAPI is well tolerated in mice, highlighting the biological safety of this therapeutic strategy.

### CTR boosts FAP-targeted $^{225}$ Ac therapy

Compared with  $^{177}$ Lu or other  $\beta$ -emitters,  $^{225}$ Ac ( $\alpha$ -emitter, 9.92 d, energy = 5.8–8.4 MeV), which has distinct radiobiological effects<sup>35</sup>, is one of the key research directions for radionuclide therapy, because its superior efficacy has been shown in the clinic<sup>36</sup>. However, owing to insufficient tumour retention, FAP-targeted  $\alpha$ -emitter therapy has not yet achieved promising therapeutic efficacy even at the preclinical stage<sup>34</sup>. We then investigated the potential of FAPI-mFS in targeted

$^{225}$ Ac therapy. Considering the long half-life and high cell-killing efficiency of  $^{225}$ Ac, a single-round treatment regimen with a 1/1,000 radioactive dose was applied as described in previous reports<sup>34,37</sup>. Of note, a dose of [ $^{225}$ Ac]Ac-FAPI-mFS (22.2 kBq) resulted in even faster tumour suppression, and a higher dose (33.3 kBq) also achieved complete tumour suppression in all mice (7/7) (Extended Data Fig. 6d–g).

Considering that FAP is a tumour microenvironment target that is expressed on cancer-associated fibroblasts<sup>12</sup>, we also established a patient-derived xenograft model derived from individuals with salivary duct carcinoma (SDC-PDX model) to further test the therapeutic efficacy of [ $^{225}$ Ac]Ac-FAPI-mFS in a more clinically relevant scenario. The expression of FAP and other key biomarkers in the SDC-PDX model was confirmed by immunohistochemistry analysis (Fig. 5a and Supplementary Fig. 23). PET/CT imaging in this PDX model suggested that the increase in tumour uptake with FAPI-mFS was still significant (Fig. 5b,c). Encouraged by these consistent results, we also performed a targeted  $\alpha$ -therapy assay with [ $^{225}$ Ac]Ac-FAPI-mFS on the PDX models (Fig. 5d–f). As expected, marked tumour suppression was observed in the group of PDX mice treated with [ $^{225}$ Ac]Ac-FAPI-mFS (Fig. 5e,f), which is consistent with the observation in the HT-1080-FAP tumour model.

We also evaluated the potential side effects of [<sup>225</sup>Ac]Ac-FAPI-mFS treatment. As shown in Extended Data Fig. 5g,i, targeted <sup>225</sup>Ac therapy may induce acute weight loss in the first few days after treatment, but the mice recover after one week. The recovery rate might be correlated with the therapeutic dose. In addition, complete blood count and blood biochemistry tests (Extended Data Fig. 6j) revealed that white blood cell and platelet counts decreased after <sup>225</sup>Ac therapy, which is not severe and is a common side effect of other radioligand therapies. Haematoxylin and eosin (H&E) staining analysis suggested that a high dose of [<sup>225</sup>Ac]Ac-FAPI-mFS might induce acute but recoverable injury in the liver and kidney (Supplementary Fig. 25).

## CTR also applies to PSMA-TRT

Owing to the high engineering capacity of heterobifunctional conjugates, it might also be possible to apply our strategy as a general tool to improve the pharmacokinetics and efficacy of other conjugates. The reported residues that can cause irreversible ligation in the SuFEx reaction include lysine, tyrosine and histidine (more than 10% of total residues), suggesting that a wide range of targets may form covalent bonds with the SuFEx warhead (Extended Data Fig. 3f). As a proof of concept, we applied this CTR strategy to engineer [<sup>177</sup>Lu]Lu-PSMA-617 (Pluvicto), which targets prostate-specific membrane antigen (PSMA) on prostate cancer cells. Through pocket analysis and molecular docking (Supplementary Table 4 and Supplementary Fig. 26), CTR-PSMA was rationally designed following the aforementioned paradigm and then synthesized (Fig. 5g and Supplementary Fig. 27). Notably, we observed significantly greater tumour uptake of [<sup>68</sup>Ga]Ga-CTR-PSMA than of [<sup>68</sup>Ga]Ga-PSMA-617 in both the LNCaP and 22RV1 cell lines, and in tumour-bearing mice (Fig. 5h and Supplementary Figs. 28 and 29). Unsurprisingly, [<sup>177</sup>Lu]Lu-CTR-PSMA, which has longer tumour retention (Supplementary Figs. 30 and 31), showed notably stronger tumour suppression than did the control (Fig. 5i and Supplementary Fig. 32). Further investigations of the structure–kinetics relationships and clinical validation of CTR-PSMAs are ongoing.

In this study, we have discovered that the tumour targeting and pharmacokinetics of radioligands can be comprehensively optimized by the use of a SuFEx-engineered linker. Our study shows that in tumour-bearing mice, a SuFEx-engineered small-molecule conjugate, such as FAPI-mFS, can increase tumour accumulation by nearly 13 times as compared with the original FAPI, and the remainder is rapidly excreted through the renal system. A pilot protein pocket screening indicated that the reactive residues are widely available in many clinically important targets. This powerful strategy will enable researchers and the pharmaceutical industry to develop tumour-targeting conjugates with small molecules, peptides, aptamers or antibody fragments.

## Online content

Any methods, additional references, Nature Portfolio reporting summaries, source data, extended data, supplementary information, acknowledgements, peer review information; details of author contributions and competing interests; and statements of data and code availability are available at <https://doi.org/10.1038/s41586-024-07461-6>.

1. Siegel, R. L., Miller, K. D., Wagle, N. S. & Jemal, A. Cancer statistics, 2023. *CA Cancer J. Clin.* **73**, 17–48 (2023).
2. Bodei, L., Herrmann, K., Schöder, H., Scott, A. M. & Lewis, J. S. Radiotheranostics in oncology: current challenges and emerging opportunities. *Nat. Rev. Clin. Oncol.* **19**, 534–550 (2022).
3. Arnold, C. Theranostics could be big business in precision oncology. *Nat. Med.* **28**, 606–608 (2022).
4. Sgouros, G., Bodei, L., McDevitt, M. R. & Nedrow, J. R. Radiopharmaceutical therapy in cancer: clinical advances and challenges. *Nat. Rev. Drug Discov.* **19**, 589–608 (2020).
5. Lai, Y. et al. Recent advances in the translation of drug metabolism and pharmacokinetics science for drug discovery and development. *Acta Pharm. Sin. B* **12**, 2751–2777 (2022).
6. Zhang, T. et al. Carrier systems of radiopharmaceuticals and the application in cancer therapy. *Cell Death Discov.* **10**, 16 (2024).
7. Sartor, O. et al. Lutetium-177-PSMA-617 for metastatic castration-resistant prostate cancer. *N. Engl. J. Med.* **385**, 1091–1103 (2021).
8. Strosberg, J. et al. Phase 3 trial of <sup>177</sup>Lu-Dotatate for midgut neuroendocrine tumors. *N. Engl. J. Med.* **376**, 125–135 (2017).
9. Boike, L., Henning, N. J. & Nomura, D. K. Advances in covalent drug discovery. *Nat. Rev. Drug Discov.* **21**, 881–898 (2022).
10. Sutanto, F., Konstantinidou, M. & Dömling, A. Covalent inhibitors: a rational approach to drug discovery. *RSC Med. Chem.* **11**, 876–884 (2020).
11. Péczka, N., Orgován, Z., Ábrányi-Balogh, P. & Keserű, G. M. Electrophilic warheads in covalent drug discovery: an overview. *Expert Opin. Drug Discov.* **17**, 413–422 (2022).
12. Hamson, E. J., Keane, F. M., Tholen, S., Schilling, O. & Gorrell, M. D. Understanding fibroblast activation protein (FAP): substrates, activities, expression and targeting for cancer therapy. *Proteomics Clin. Appl.* **8**, 454–463 (2014).
13. Jansen, K. et al. Extended structure–activity relationship and pharmacokinetic investigation of (4-quinolinoyl)glycyl-2-cyanopyrrolidine inhibitors of fibroblast activation protein (FAP). *J. Med. Chem.* **57**, 3053–3074 (2014).
14. Kratochwil, C. et al. <sup>68</sup>Ga-FAPI PET/CT: tracer uptake in 28 different kinds of cancer. *J. Nucl. Med.* **60**, 801–805 (2019).
15. Li, M., Younis, M. H., Zhang, Y., Cai, W. & Lan, X. Clinical summary of fibroblast activation protein inhibitor-based radiopharmaceuticals: cancer and beyond undefined. *Eur. J. Nucl. Med. Mol.* **49**, 2844–2868 (2022).
16. Wen, X. et al. Evans blue-modified radiolabeled fibroblast activation protein inhibitor as long-acting cancer therapeutics. *Theranostics* **12**, 422–433 (2022).
17. Wang, Y.-H., Zhang, F., Diao, H. & Wu, R. Covalent inhibition mechanism of antidiabetic drugs—vildagliptin vs saxagliptin. *ACS Catal.* **9**, 2292–2302 (2019).
18. Xu, M. et al. Albumin binder-conjugated fibroblast activation protein inhibitor radiopharmaceuticals for cancer therapy. *J. Nucl. Med.* **63**, 952–958 (2022).
19. Zhang, P. et al. Fatty acid-conjugated radiopharmaceuticals for fibroblast activation protein-targeted radiotherapy. *Eur. J. Nucl. Med. Mol. Imaging* **49**, 1985–1996 (2022).
20. Dong, J., Krasnova, L., Finn, M. G. & Sharpless, K. B. Sulfur(VI) fluoride exchange (SuFEx): another good reaction for click chemistry. *Angew. Chem. Int. Ed.* **53**, 9430–9448 (2014).
21. Grimster, N. P. et al. Aromatic sulfonyl fluorides covalently kinetically stabilize transthyretin to prevent amyloidogenesis while affording a fluorescent conjugate. *J. Am. Chem. Soc.* **135**, 5656–5668 (2013).
22. Baranczak, A. et al. A fluorogenic aryl fluorosulfate for intraorganellar transthyretin imaging in living cells and in *Caenorhabditis elegans*. *J. Am. Chem. Soc.* **137**, 7404–7414 (2015).
23. Li, Q. et al. Developing covalent protein drugs via proximity-enabled reactive therapeutics. *Cell* **182**, 85–97 (2020).
24. Sun, W. et al. Genetically encoded chemical crosslinking of RNA in vivo. *Nat. Chem.* **15**, 21–32 (2023).
25. Li, S., Wang, N., Yu, B., Sun, W. & Wang, L. Genetically encoded chemical crosslinking of carbohydrate. *Nat. Chem.* **15**, 33–42 (2023).
26. Zheng, Q. et al. Sulfur [<sup>18</sup>F]fluoride exchange click chemistry enabled ultrafast late-stage radiosynthesis. *J. Am. Chem. Soc.* **143**, 3753–3763 (2021).
27. Liu, Z. et al. SuFEx Click chemistry enabled late-stage drug functionalization. *J. Am. Chem. Soc.* **140**, 2919–2925 (2018).
28. Fleming, F. F., Yao, L., Ravikumar, P. C., Funk, L. & Shook, B. C. Nitrile-containing pharmaceuticals: efficacious roles of the nitrile pharmacophore. *J. Med. Chem.* **53**, 7902–7917 (2010).
29. Backus, K. M. et al. Proteome-wide covalent ligand discovery in native biological systems. *Nature* **534**, 570–574 (2016).
30. Willemsen-Seegers, N. et al. Compound selectivity and target residence time of kinase inhibitors studied with surface plasmon resonance. *J. Mol. Biol.* **429**, 574–586 (2017).
31. De Cesco, S., Kurian, J., Dufresne, C., Mittermaier, A. K. & Moitessier, N. Covalent inhibitors design and discovery. *Eur. J. Med. Chem.* **138**, 96–114 (2017).
32. Giovanella, L. et al. EANM practice guideline for PET/CT imaging in medullary thyroid carcinoma. *Eur. J. Nucl. Med. Mol. Imaging* **47**, 61–77 (2020).
33. Zha, Z. et al. New PSMA-targeting ligands: transformation from diagnosis (Ga-68) to radionuclide therapy (Lu-177). *J. Med. Chem.* **65**, 13001–13012 (2022).
34. Liu, Y. et al. Fibroblast activation protein targeted therapy using [<sup>177</sup>Lu]FAPI-46 compared with [<sup>225</sup>Ac]FAPI-46 in a pancreatic cancer model. *Eur. J. Nucl. Med. Mol. Imaging* **49**, 871–880 (2022).
35. Group, T.A.T.W. Targeted alpha therapy, an emerging class of cancer agents: a review. *JAMA Oncol.* **4**, 1765–1772 (2018).
36. Kratochwil, C. et al. <sup>225</sup>Ac-PSMA-617 for PSMA-targeted α-radiation therapy of metastatic castration-resistant prostate cancer. *J. Nucl. Med.* **57**, 1941–1944 (2016).
37. Watabe, T. et al. Theranostics targeting fibroblast activation protein in the tumor stroma: <sup>64</sup>Cu- and <sup>225</sup>Ac-labeled FAPI-04 in pancreatic cancer xenograft mouse models. *J. Nucl. Med.* **61**, 563–569 (2020).

**Publisher's note** Springer Nature remains neutral with regard to jurisdictional claims in published maps and institutional affiliations.

Springer Nature or its licensor (e.g. a society or other partner) holds exclusive rights to this article under a publishing agreement with the author(s) or other rightsholder(s); author self-archiving of the accepted manuscript version of this article is solely governed by the terms of such publishing agreement and applicable law.

© The Author(s), under exclusive licence to Springer Nature Limited 2024

## Methods

### Statistics and reproducibility

No statistical methods were used to predetermine sample size. The experiments were not randomized and investigators were not blinded to allocation during experiments and outcome assessment.

### Chemical reagents and antibodies

The synthesis and characterization of compounds **1** to **8** are detailed in the Supplementary Methods. AF488 NHS ester was from MCE (HY-D1730). Recombinant hFAP (10464-H07H), DPP-4/CD26 (10688-H08H) and hPSMA (15877-H07H-B) were from Sino Biological. Recombinant hPREP (4308-SE) and mFAP (8647-SE) were from Bio-Techne. Other chemical reagents and solvents were sourced from Bide Pharmatech, J&K Scientific, Energy Chemical or Thermo Fisher Scientific. Nuclear magnetic resonance spectra were recorded at room temperature using a Bruker Avance 400-MHz spectrometer. Signals are reported in parts per million (ppm), with signal multiplicity denoted as single (s), broad (br), doublet (d), triplet (t), quartet (q) or multiplet (m); coupling constants are measured in hertz (Hz). ‘Chemistry yields’ pertain to the weight of the isolated pure chemicals. [<sup>68</sup>Ge]GaCl<sub>3</sub> was obtained using a 0.6 M hydrochloric acid solution from the <sup>68</sup>Ge–<sup>68</sup>Ge generator provided by iThemba LABS. [<sup>177</sup>Lu]LuCl<sub>3</sub> was generated through a 14-MeV proton cyclotron of our laboratory. [<sup>177</sup>Lu]LuCl<sub>3</sub>, in a 0.1 M hydrochloric acid solution, was purchased from ITG. [<sup>225</sup>Ac]Ac(NO<sub>3</sub>)<sub>3</sub> was from Oak Ridge National Laboratory. For immunohistochemistry analysis, the antibodies were from Abcam, specified by clone and dilution ratio: anti-FAP (RM1080, 1:50), anti-calcitonin (EPR68(2), 1:100), anti-synaptophysin (YE269, 1:100), anti-CEA (EPR20721, 1:100), anti-CGA (RM1025, 1:100), anti-AE1/AE3 (C-11, 1:100), anti-cytokeratin 5/6 (LP34, 1:100) and anti-cytokeratin 7 (SP52, 1:100). For more information on essential materials and instruments, see the Supplementary Information.

### Synthesis and isolation of compounds **1** to **7**

The synthetic routes for compounds **1** to **7** are depicted in Supplementary Figs. 2–4 (ref. 18). For the synthesis of compound **3**, to a solution of **int 3** (8.4 mg, 7.2 µmol) in DMF (200 µl), commercially available **1c** (8.6 µmol, 1.2 equiv.), DIPEA (21.6 µmol, 3.0 equiv.) and HBTU (8.6 µmol, 1.2 equiv.) were added and the reaction mixture was stirred at 25 °C for 30 min. The reaction solution was concentrated under reduced pressure to remove the solvent. TFA (1.0 ml) was added and the mixture was reacted at 25 °C for 3 h. The crude product was purified by HPLC to get compound **3** (7.5 mg, 85% yield). The other compounds were synthesized using a similar method to that described for compound **3**. Both HPLC–mass spectrometry and high-resolution mass spectrometry were used to assess the quality of compounds **1**–**7**.

### Molecular docking and analysis of binding-pocket residues

Docking was performed using GOLD v.2022.3.0. The original structures of FAP (PDB: 1Z68) and PSMA (PDB: 5O5T) were prepared by removing waters and ions followed by constrained minimization. The atomic coordinates of the Lu-DOTA complex for reference (Supplementary Fig. 6) are available in the Cambridge Structural Database with identifier NOJYIU. The initial conformations of FAP ligands were generated and optimized according to the MMFF94 force field within RDKit. For FAP, the covalent docking protocol in GOLD was used. For PSMA, the similar ligand co-crystal structure (PDB: 5O5T) was used as a template. One hundred docking poses of each ligand were generated, of which the best-scored pose was selected. With regard to the binding pockets of FAPI-04 in FAP and that of PSMA-617 in PSMA, various parameters of each residue of interest were calculated using the pocket residue analysis module in MOE 2020. Modelled protein–ligand complexes from docking or MD simulations results were loaded into Discovery

Studio (BIOVIA) to generate two-dimensional ligand–residue interaction profiles.

### MD simulations

MD simulations were performed with AMBER 2020 (ref. 38). Simulation inputs were generated in tleap, in which docked complexes with covalent linkage at S624 were solvated with water (TIP3P model), neutralized and parameterized with the ff19SB and gaff2 force fields. Additional parameters of ligands were generated in antechamber with the AM1-BCC force field. MD simulations were performed on GPUs using the pmemd.cuda module. After minimization, each system was heated from 0 K to 300 K under the NVT ensemble over 20 ps. Then, another 200-ps equilibration at 300 K and a pressure of 1.0 bar was performed in the NPT ensemble using a Langevin thermostat. A 150-ns production run under the NPT ensemble at 300 K was performed for each model applying periodic boundary conditions. All hydrogen-containing bonds during the MD simulations were constrained using SHAKE. A cut-off of 12 Å was set for nonbonded interactions. The CPPTRAJ module was used to analyse MD trajectory data. For the two models with higher stability, the FS warhead of each ligand was bonded with the corresponding tyrosine. The resulting models underwent another 50-ns NPT simulation.

### Radiolabelling

Radiolabelling was generally achieved by incubating vectors (around 10 µM) with radionuclides at specific pH and temperature (Supplementary Table 1). Each reaction was monitored by radio-HPLC or radio-thin-layer chromatography. Notably, fresh samples containing <sup>225</sup>Ac were allowed to rest for at least five hours to reach secular equilibrium before thin-layer chromatography analysis.

### Enzyme activity assay

Enzyme activity was measured kinetically in a 200 µl volume at 37 °C, by tracking the initial rates of p-nitroanilide release (absorption at 405 nm) from the substrate at various time points. This was done using a Victor X5 Multilabel Reader, as previously described<sup>13</sup> (Supplementary Table 5). Half-maximum inhibitory concentration (IC<sub>50</sub>) values were determined using GraphPad v.9.0, fitting the data to an inhibitory dose–response equation.

### Autoradioluminography

The preparation of samples for SDS–PAGE is described in the Supplementary Methods. The gel from SDS–PAGE was placed against a phosphor screen inside a cassette for exposure (Supplementary Fig. 37). After removing the gel in a light-proof setting, the phosphor screen underwent autoradioluminography at a suitable voltage. The appropriate voltage for each experiment was verified through a quality control curve, correlating radioactivity to the greyscale of bands at each time point to ensure response linearity. Subsequently, the gels were stained with Coomassie blue to show the bands of proteins for co-location.

### Tandem mass spectrometry

For in vitro ligation, each of the <sup>nat</sup>Lu-CTR-FAPIs (4 µM, prepared with [<sup>nat</sup>Lu]LuCl<sub>3</sub> using protocols analogous to <sup>177</sup>Lu-labelling) was incubated with recombinant hFAP (4 µg, 4 µM) in PBS buffer (0.01 M, pH 7.4) at 37 °C for 24 h. The mixtures were then separated by 10% SDS–PAGE before the Coomassie brilliant blue stain. The bands corresponding to each ligated complex were cut out guided by the mass shift of hFAP and decolourized in a 1:1 H<sub>2</sub>O–acetonitrile (ACN) solution with NH<sub>4</sub>HCO<sub>3</sub> (100 mM) until transparent. After dehydration in ACN at 37 °C, the samples were reduced (10 mM DTT and 100 mM NH<sub>4</sub>HCO<sub>3</sub>, 56 °C, 30 min) and alkylated (55 mM iodoacetamide and 100 mM NH<sub>4</sub>HCO<sub>3</sub>, room temperature, 30 min) in the dark. This was followed by dehydration (ACN) and digestion (20 ng µl<sup>-1</sup> trypsin, 20 ng µl<sup>-1</sup> chymotrypsin, 100 mM NH<sub>4</sub>HCO<sub>3</sub> and 1 mM CaCl<sub>2</sub>, at 25 °C for 12 h, then at

37 °C for 6 h). The resulting peptides were extracted three times with an extraction buffer (50% ACN, 45% H<sub>2</sub>O and 5% formic acid) and then concentrated to dryness under vacuum. After desalting with Pierce C18 tips (Thermo Fisher Scientific, 87784) and drying by vacuum centrifugation, all samples were resuspended in deionized water with 0.1% FA and analysed using a Thermo Scientific Q Exactive Plus Orbitrap mass spectrometer coupled with an Easy-nLC II HPLC. Mass spectrometry raw data were analysed using pFind (Supplementary Fig. 41) to identify the ligation sites.

## SPR

SPR was performed referring to a previously reported method<sup>30</sup>. FAP was immobilized onto a Series S Sensor Chip CM5. Subsequently, a pre-run was performed for at least 30 min at a flow rate of 30 µl per min at 25 °C to achieve surface stability, which was followed by a buffer injection and five consecutive injections of each tested compound at increasing concentrations. Each injection was processed at a flow rate of 30 µl per min with an association time of 100 s per concentration and a dissociation time of 1,800 s. The kinetic constants of tested compounds were determined by single-cycle kinetics. SPR sensorgrams were analysed with Biacore Evaluation Software using a method of double referencing. The resulting curves were fitted into either the 1:1 binding model or the two-state reaction model and the best-fit model for each curve was selected.

## Cell culture

The human fibrosarcoma cells from the American Type Culture Collection transferred with the human FAP gene (HT-1080-FAP) were customized by WuXi Biologics, and cultured in Eagle's minimum essential medium containing 10% fetal bovine serum (FBS), 1% antibiotic–antimycotic and 4 µg ml<sup>-1</sup> blasticidin S (InvivoGen). LNCaP and 22RV1 cells were obtained from the American Type Culture Collection, and cultured in RPMI 1640 medium supplemented with 10% FBS and 1% streptomycin–penicillin. All cells were regularly tested for mycoplasma contamination and cultured or incubated (as in cell-based assays) in a 5% CO<sub>2</sub> incubator at 37 °C.

## Cell-based competitive binding, uptake and efflux assays

IC<sub>50</sub> values of the CTR-FAPIs (at gradient concentrations from 10<sup>-6</sup> to 10<sup>-10</sup> M) were measured by competitive binding with [<sup>68</sup>Ga]Ga-FAPI-04 ( $A_m > 37 \text{ MBq nmol}^{-1}$ , 0.75 nM) in the HT-1080-FAP cell line as previously reported<sup>18</sup>.

For radiometric assays, cells in six-well plates were incubated with <sup>68</sup>Ga-labelled RLCs ( $A_m > 37 \text{ MBq nmol}^{-1}$ , 1 nM) in a serum-free medium. Cellular uptake was terminated at each indicated time point by removing the medium and washing the cells twice with cold PBS. Cells were then lysed with lysis buffer (0.3 M NaOH, 0.2% SDS) before being measured for radioactivity. For cellular efflux evaluation, the medium with RLCs was substituted with fresh medium with 1% FBS after a one-hour incubation. At each indicated time point, the medium was collected and measured for its radioactivity.

For the fluorescent assay, cells were seeded in 35-mm confocal dishes and incubated with compounds 6 or 7 (100 nM) in the dark for 2 h. After this, the cells were washed twice with HBSS (pH 7.4). They were then cultured in a fresh medium containing 1% FBS in the dark. At each specified time point, the cells underwent two washes with 1 ml PBS and were then incubated with DAPI (100 nM) for 10 min, followed by a 10-min fixation in 4% paraformaldehyde solution. Fluorescence was observed at room temperature using a Nikon A1R-si Laser scanning confocal microscope with a 20× objective lens. The relative fluorescence intensity was measured using ImageJ.

## Animal ethics and general protocols of animal studies

All mouse studies were conducted following the principles and procedures outlined in the Guide for the Care and Use of Laboratory

Animals (Ministry of Health, China) and the protocol was approved by the Institutional Animal Care and Use Committee (IACUC) of Peking University (IACUC ID: CCME-LiuZB-1). The tumour-bearing mice were subjected to the indicated treatments and small-animal PET studies when the tumour volume reached 100 mm<sup>3</sup> (about one week after inoculation) and 200–500 mm<sup>3</sup> (two to three weeks after inoculation), respectively. Ethical compliance with the IACUC protocol was maintained. In none of the experiments did the size of the tumour graft surpass 2 cm in any two dimensions (according to the limits defined by the IACUC protocol), and no mouse had severe abdominal distension (an increase of 10% or more in original body weight in the short term).

## PET/CT and SPECT/CT imaging

PET/CT and single-photon emission computed tomography (SPECT)/CT imaging for mice were performed on a Mediso nanoScan PET 122S or InViView-3000B PET/SPECT/CT imaging system with mice injected with RLCs through the tail vein. Mice were anaesthetized with isoflurane in oxygen 10 min before each imaging time point. Standard data acquisition and image reconstruction of the PET or SPECT data were performed, generating maximum intensity projection images. Volumes of the tumour and major organs were delineated, from which the tracer uptake was calculated in the unit of %ID g<sup>-1</sup>. The data analysis was performed on Interview Fusion software (v.3.09.008.0000).

For clinical studies, PET/CT was performed on a total-body PET/CT (uEXPLORER) with two patients with MTC, who were treated successively with [<sup>68</sup>Ga]Ga-FAPI-04 and [<sup>68</sup>Ga]Ga-FAPI-mFS ( $A_m \approx 11.2 \text{ MBq nmol}^{-1}$ ; around 3.7 MBq kg<sup>-1</sup>) with an interval of 24 h. Regions of interest were selected and the corresponding tracer uptake was calculated as the SUV<sub>max</sub> value with 3D Slicer. Regions with an uptake higher than background activity were considered pathological. The T/N ratio was calculated as (SUV<sub>max</sub>)<sub>tumour</sub> / (SUV<sub>max</sub>)<sub>normal</sub>.

## Biodistribution study

HT-1080-FAP cell-line-derived xenograft (CDX) mouse models ( $n = 7$ , tumour size of around 150 mm<sup>3</sup>) were intravenously injected with RLCs and then euthanized at different time points after injection. Major organs and tissues were collected in EP tubes and weighed. A WIZARD2 2480 automatic γ-counter was used to measure the radioactivity of each sample, from which the corresponding uptake (%ID g<sup>-1</sup>) was further calculated.

## Radiation dosimetry

Internal dosimetry estimates were calculated using the organ-level internal dose assessment (OLINDA) software v.2.1 (ref. 39). These estimates were performed using the 25g MOBY phantom for mice, the NURBS model for adult males and the previously reported unit density sphere model for tumours. All phantoms and the sphere model are available in OLINDA and require the input of the total number of decays normalized by injected activity in units of (MBq×h) MBq<sup>-1</sup> for each of the source organs or tumours. More details are provided in the Supplementary Methods.

## Preclinical TRT

Various CDX or PDX mouse models from the same batch were randomized into groups when the average tumour size reached around 100 mm<sup>3</sup>. Indicated <sup>177</sup>Lu- or <sup>225</sup>Ac-labelled RLCs were administered to treated groups following the regimens described in Supplementary Tables 12 and 13. The long diameter ( $L$ ) and short diameter ( $W$ ) of tumours and the body weight of mice were monitored every two to three days. The tumour volume was determined using the formula for an ellipsoid ( $V = 1/2 \times L \times W^2$ ). For the Kaplan–Meier curve analysis, mice were euthanized and counted towards the mortality end-point when their tumours exceeded 1,500 mm<sup>3</sup>.

# Article

## Human ethics and general protocols of clinical studies

We conducted a prospective, single-centre, open-labelled clinical trial, aiming to evaluate the clinical value of CTR-FAP1<sup>68</sup>Ga-PET-CT in malignant tumours. The study was approved by the Ethics Review Committee of Peking University Cancer Hospital and Institute (2023YJZ20) and was registered at clinicaltrials.gov (NCT06084767). The pilot results from two patients with MTC are presented in this work.

## Reporting summary

Further information on research design is available in the Nature Portfolio Reporting Summary linked to this article.

## Data availability

The structural coordinates of proteins for analysis are available in the PDB with accession codes 1L5G, 7T11, 1Z68 and 5OST. All other data supporting the findings of this study are included in the Article and its Supplementary Information. Source data are provided with this paper.

38. Weiner, P. K. & Kollman, P. A. AMBER: assisted model building with energy refinement. A general program for modeling molecules and their interactions. *J. Comput. Chem.* **2**, 287–303 (1981).
39. Stabin, M. G., Sparks, R. B. & Crowe, E. OLINDA/EXM: the second-generation personal computer software for internal dose assessment in nuclear medicine. *J. Nucl. Med.* **46**, 1023–1027 (2005).

**Acknowledgements** We thank C. Wang, X. Wang, W. Zhou and X. Liu for experimental assistance with tandem mass analysis; S. Huang and L. Ma for assistance with

autoradioluminography; Q. Wang for experimental assistance with SPR; C. Pan for assistance with computational studies; and L. Lai for suggestions on the manuscript. The high-resolution mass-spectrometry and confocal-imaging measurements were performed at the Analytical Instrumentation Center of Peking University. This study was funded by the National Natural Science Foundation of China (NSFC, grant 22225603), the Ministry of Science and Technology of the People's Republic of China (grant 2021YFA1601400), the Beijing Municipal Natural Science Foundation (grant Z200018) to Z. Liu, the Program of the Local Science and Technology Development (Gansu province, grant YDZX20216200001201) to X.-Y.C., Peking University Clinical Scientist Training Program (grant BMU2024PYJH006) to Z. Li, the NSFC grant 32301152 and the Beijing Natural Science Foundation (grant 7232351) to Z.K., the NSFC grant 82071967 to L.H., the Capital's Funds for Health Improvement and Research (grant 2022-ZZ-2154) to Z.Y.

**Author contributions** Z. Liu conceived the study. Z. Liu and X.-Y.C. performed the molecular design. X.-Y.C., assisted by Y. Liu, Z.W., C.W. and J.G., performed the chemical analysis, characterization and in vitro studies. Z. Li and Z.K. performed the clinical study. X.-Y.C., assisted by Y. Liu, Z.W. and M.X., performed the radiolabelling, PET imaging and therapy studies. H.M., Y. Li and X.-Y.C. performed the theoretical calculation. J.C. produced <sup>86</sup>Y and assisted X.-Y.C. with the dosimetry. S.L., Z.Y., L.H., W.Z. and Z.H. provided suggestions for the clinical study. X.-Y.C., Z. Liu, Z.K. and Z. Li analysed the data. Z. Liu and X.-Y.C. wrote the manuscript with input from all authors. All authors discussed the results and commented on the manuscript.

**Competing interests** Z. Liu and X.-Y.C. are co-inventors on a relevant patent application (PCT/CN2023/096111) filed by Peking University, and a relevant provisional patent application (PCT/CN2023/096106) filed by Changping Laboratory. Z. Liu is a co-founder of and scientific advisor for BoomRay Pharmaceuticals. The remaining authors declare no competing interests.

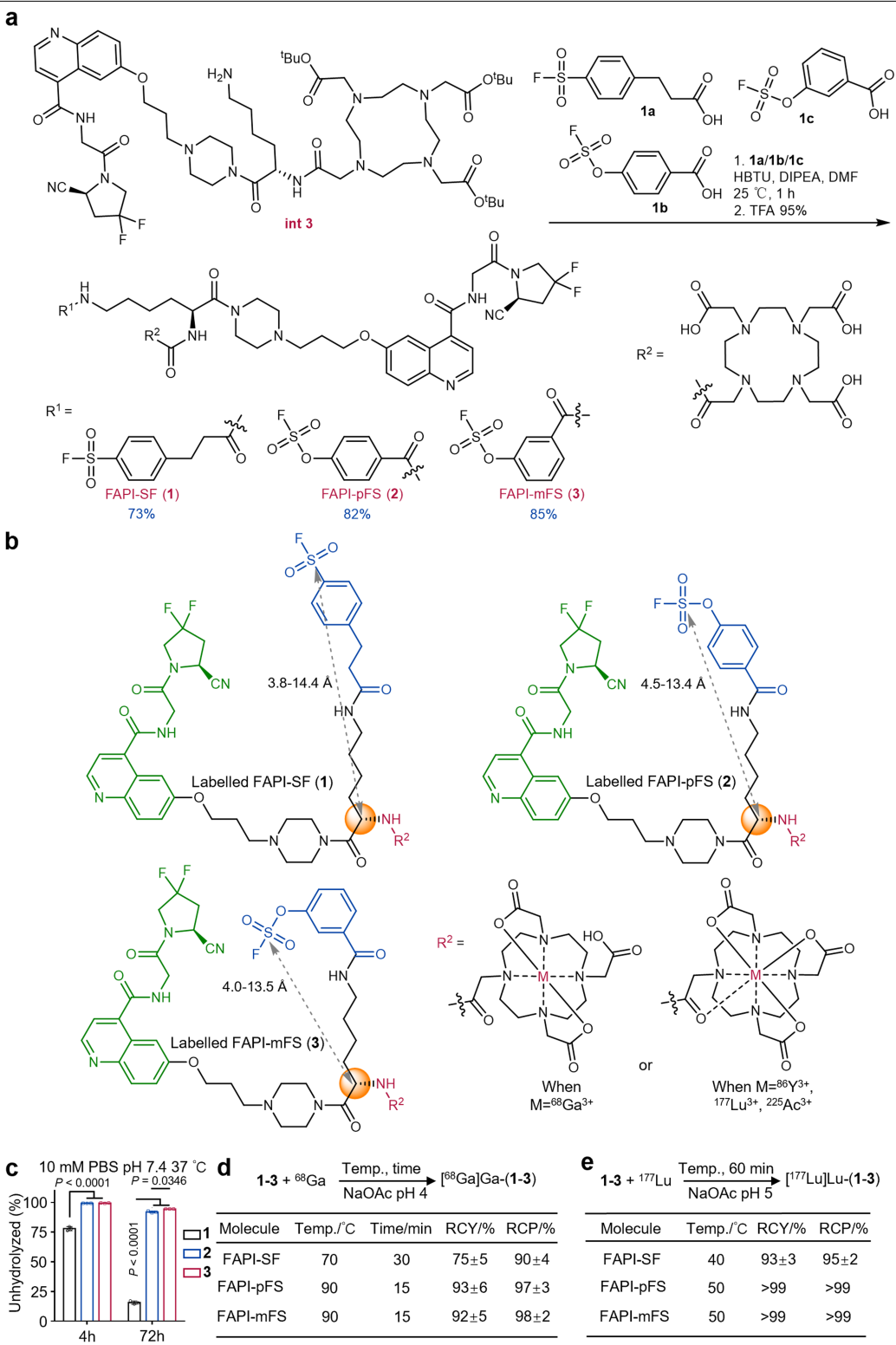
## Additional information

**Supplementary information** The online version contains supplementary material available at <https://doi.org/10.1038/s41586-024-07461-6>.

**Correspondence and requests for materials** should be addressed to Zhibo Liu.

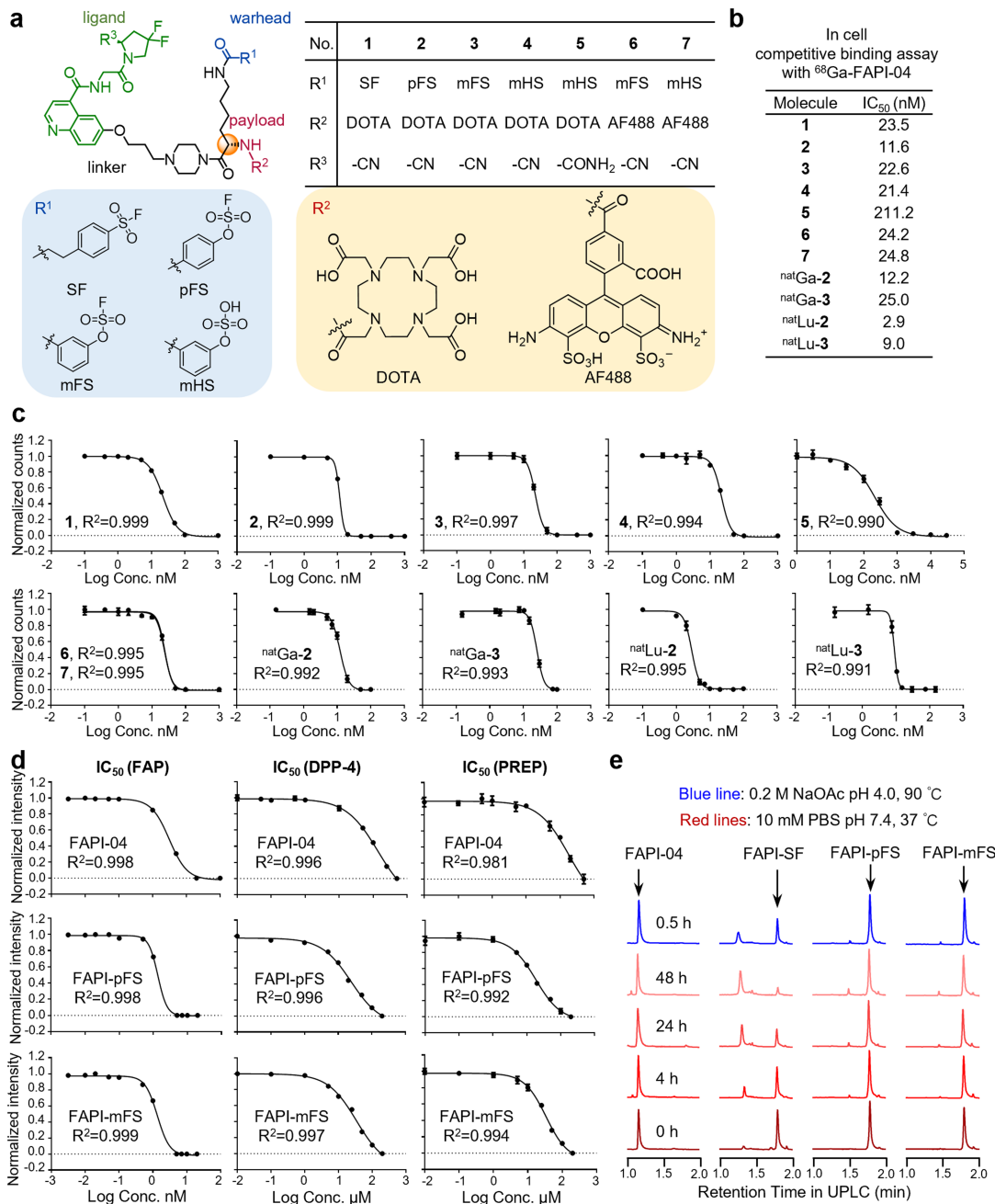
**Peer review information** *Nature* thanks Alvaro Lorente-Macias, Jessie Nedrow, Asier Unciti-Broceta and the other, anonymous, reviewer(s) for their contribution to the peer review of this work.

**Reprints and permissions information** is available at <http://www.nature.com/reprints>.



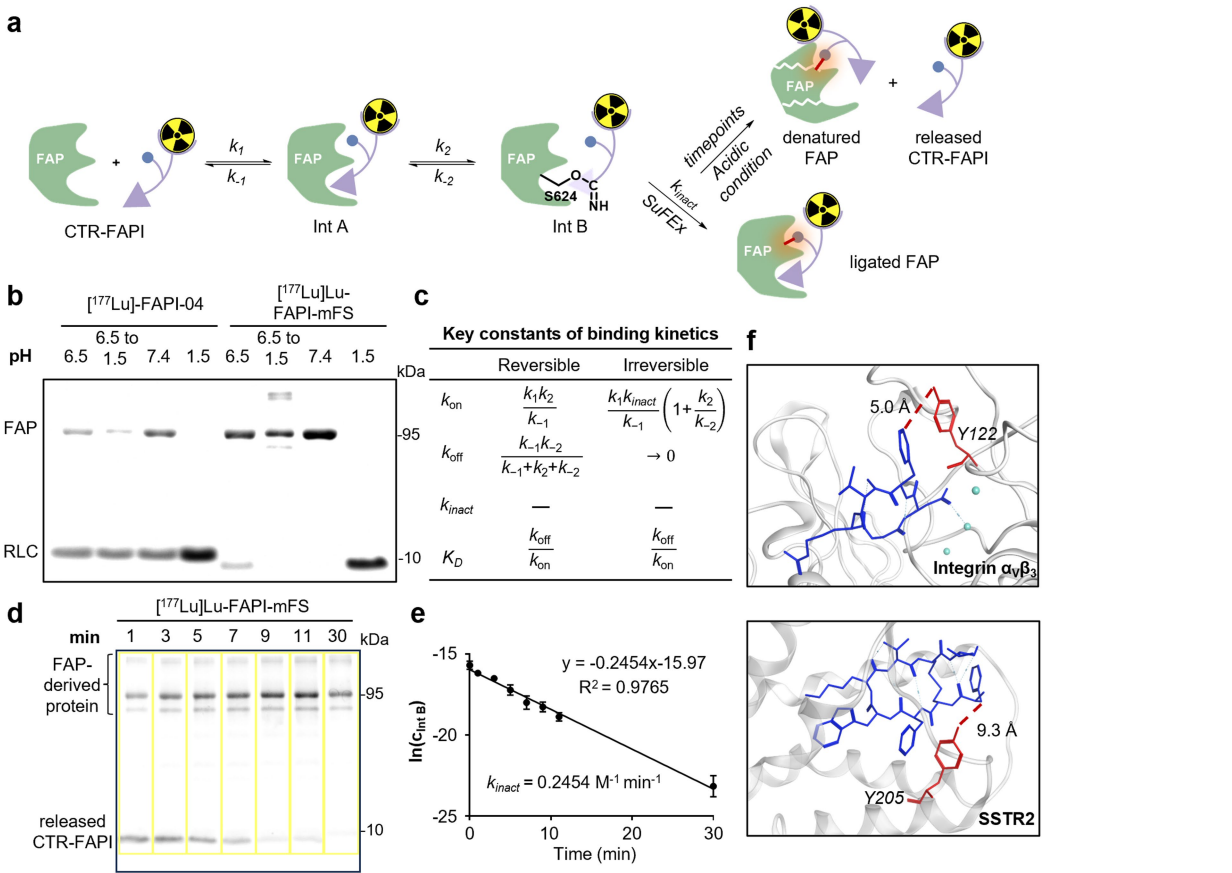
**Extended Data Fig. 1 | Synthetic routes for the CTR-FAPI vectors and their radiolabelling.** **a**, Synthetic route or FAP-targeting CTRs in this work. **b**, Chemical structure of the radiolabelled CTR-FAPIs. The grey lines show the minimum and maximum distance between the modification starting carbon and the sulfur (VI) calculated by MOE. **c**, Quantitative comparison of the

stability of  ${}^{177}\text{Lu}$ -labelled CTR-FAPIs by radio-HPLC.  $n = 3$ , mean  $\pm$  s.d. is depicted, one-way ANOVA followed by Tukey's multiple comparison test. **d**, Condition and results of  ${}^{68}\text{Ga}$ -labelling. **e**, Condition and results of  ${}^{177}\text{Lu}$ -labelling. See SI for  ${}^{66}\text{Y}$  and  ${}^{225}\text{Ac}$  radiolabelling details.



**Extended Data Fig. 2 | Chemical structures, target affinity and stability profile of CTR-FAPIs and related molecules.** **a**, Chemical structures of the CTR-FAPI vectors and fluorescent probes discussed in this work. **b**, IC<sub>50</sub> values obtained by in-cell competitive binding assay with <sup>68</sup>Ga-FAPI-04. Every test was performed at least twice individually. **c**, Representative IC<sub>50</sub> curves of FAPI-04, FAPI-pFS and FAPI-mFS competing with <sup>68</sup>Ga-FAPI-04 to bind

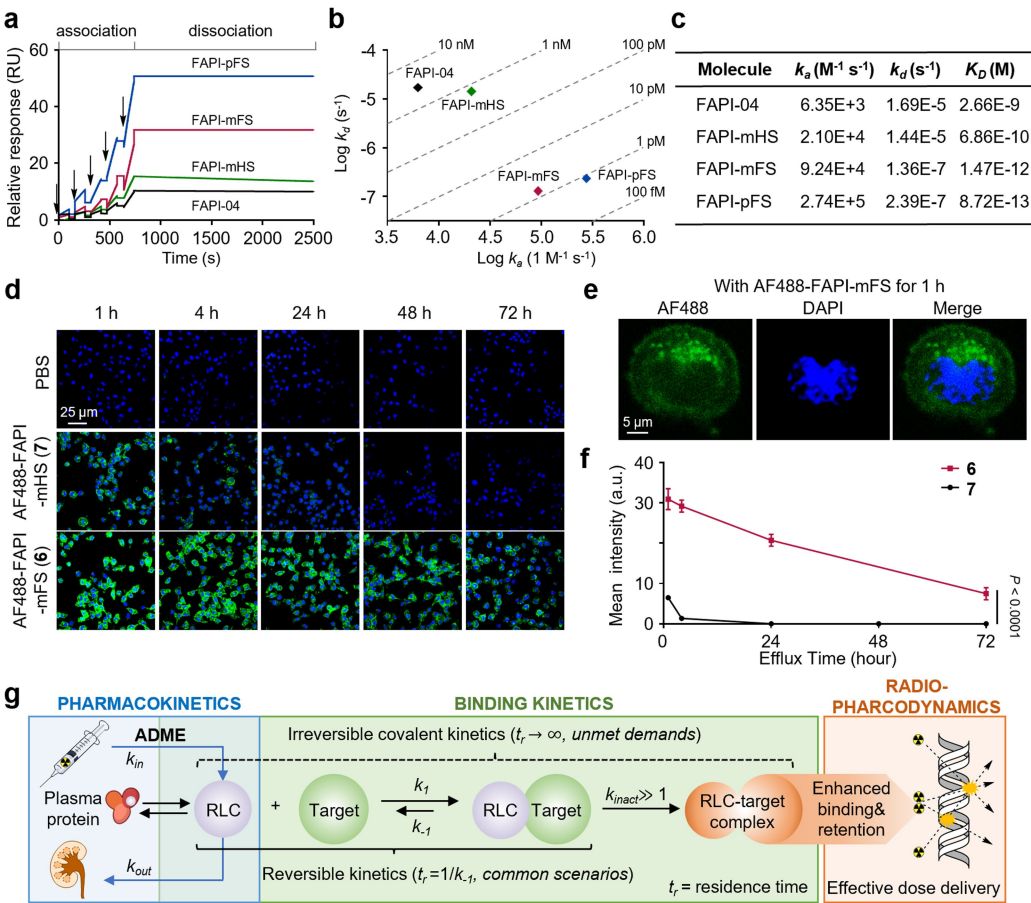
HT-1080-FAP cells ( $n = 4$ ). **d**, Representative IC<sub>50</sub> curves of FAPI-04, FAPI-pFS and FAPI-mFS tested in enzyme activity inhibition assays to evaluate the FAP binding selectivity ( $n = 4$ ). **e**, Evaluation of the stability of FAPI-SF, FAPI-pFS and FAPI-mFS vectors under common <sup>68</sup>Ga-labelling condition or physiological condition by UPLC. Data are mean  $\pm$  s.d. (c,d).



#### Extended Data Fig. 3 | Further study of the covalent binding mechanism.

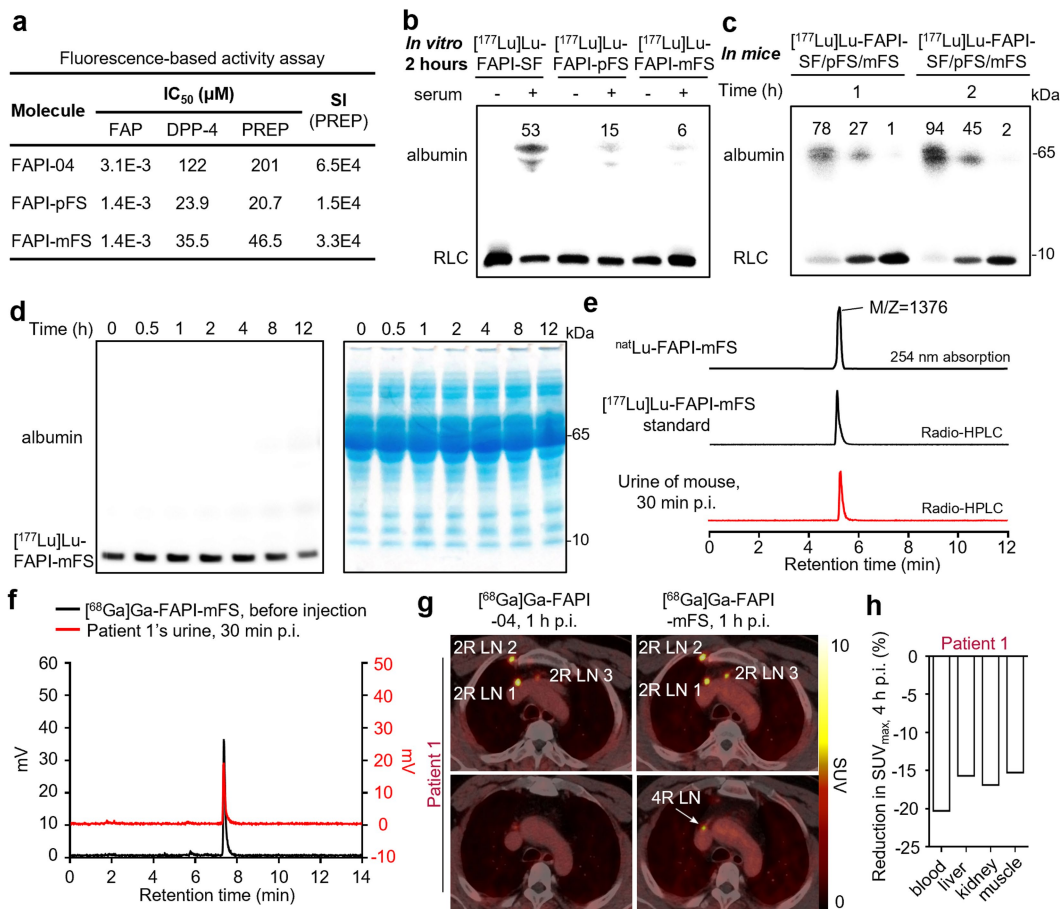
**a**, Proposed kinetic process of CTR-FAPIs binding to FAP based on experimental results and literature evidence. **b**, Control experiment suggesting FAPI-04 forms a reversible acid-sensitive covalent bond with FAP, while CTR-FAPIs, e.g., FAPI-mFS (**3**), forms an irreversible covalent bond. **c**, Key kinetic constants obtained by theoretical derivation are concluded. **d,e**, Investigation of the irreversible binding rate ( $k_{inact}$ ) between [<sup>177</sup>Lu]-FAPI-mFS and FAP by

autoradioluminography-based kinetic study (**d**). Data are mean  $\pm$  s.d. (**e**). Lane splits are shown by yellow boxes.  $C_{int\_B}$ , the concentration of Int B at the moment. **f**, Y122 at Integrin  $\alpha_v\beta_3$  (PDB: 1L5G) (above). The cyan spheres are  $Mn^{2+}$ . Y205 at SSTR2 (PDB: 7T11) (below); proteins are in grey; ligands are in blue and the selected potential residues for covalent binding are in red. Data are representative of two (**b**) or three (**d**) independent experiments.



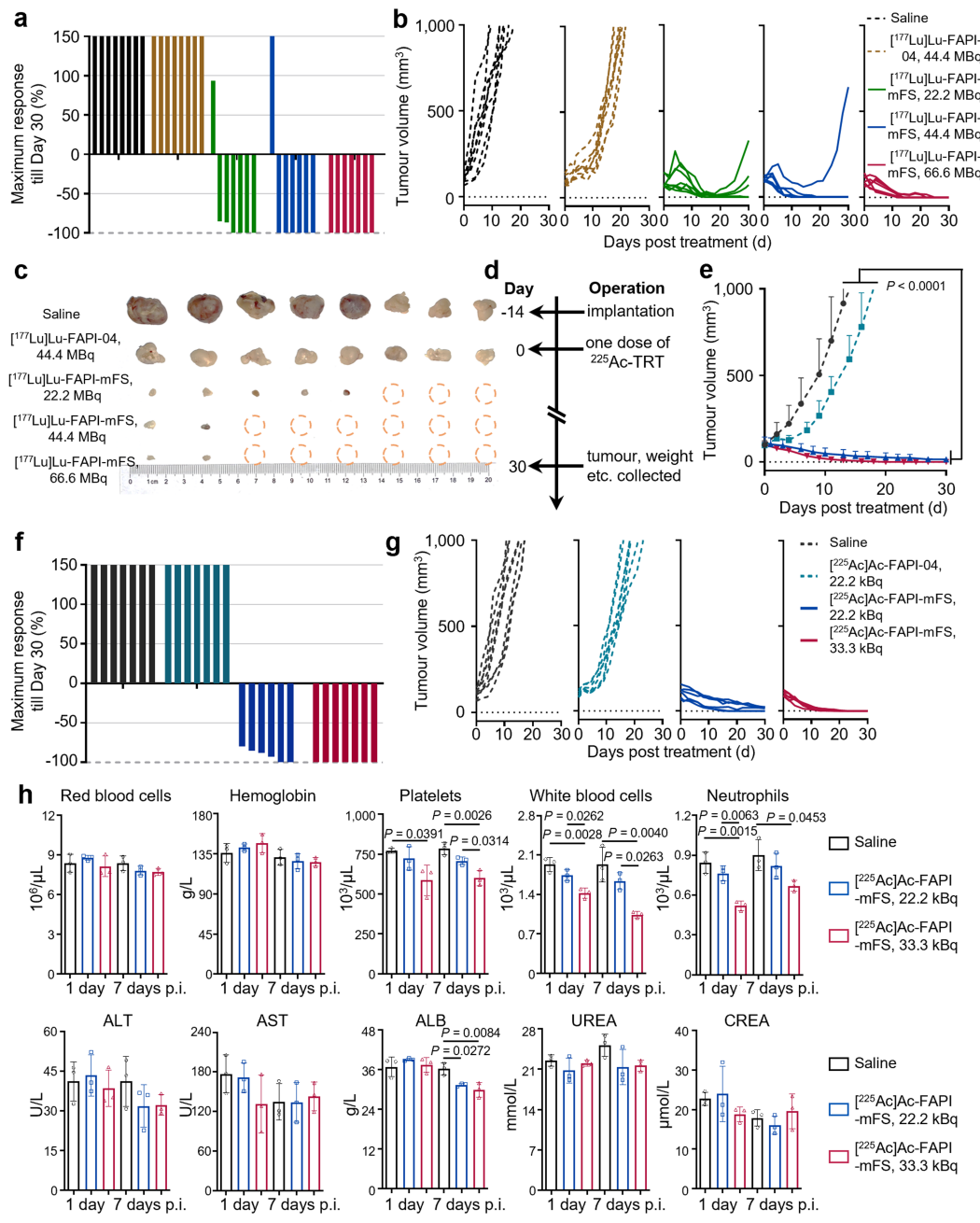
**Extended Data Fig. 4 | Additional pharmacological insights on CTR-FAPIs.**  
**a–c**, Surface plasmon resonance (SPR) analysis of FAPI-04 (black), FAPI-pFS (blue), FAPI-mFS (red) and FAPI-mHS (green) binding to FAP, respectively. **a**, SPR sensograms of the single-cycle kinetics. The arrows refer to the subsequent injections in the association phase. RU, resonance units. **b**, Plot of the association rate (x-axis) and dissociation rate (y-axis) based on SPR. **c**, Summary of kinetic constants according to SPR assay. **d**, Representative confocal fluorescence images of visualizing the cellular efflux of FAPI-mFS-AF488 probe (**6**) and its FS-hydrolysed control (**7**). The HT-1080-FAP cells were pre-treated with fluorescent probes **6** or **7** (10  $\mu$ M in MEM medium) for 2 h,

followed by incubation with probe-free medium for 1–72 h; scale bar = 25  $\mu$ m. **e**, Representative confocal fluorescence images showing the localization of probe **6** in cell; DAPI = 4',6-diamidino-2-phenylindole, for DNA staining; scale bar = 5  $\mu$ m. **f**, Fluorescence intensity analysis in HT-1080-FAP cells according to the examined field of view by confocal microscopy ( $n = 3$  fields). Mean  $\pm$  s.d. is depicted. Data at 72 h are analysed by two-tailed unpaired Student's *t*-test. **g**, Schematic relationship between pharmacokinetics, binding kinetics and radio-pharmacodynamics for radiopharmaceuticals in the dynamic blood flow scenario. Data are representative of two independent experiments. The illustrations in **g** were created with BioRender.



**Extended Data Fig. 5 | Binding selectivity and metabolic stability of CTR-FAPIs.** **a**, IC<sub>50</sub> summary of FAPI-04, FAPI-pFS or FAPI-mFS inhibiting FAP, DPP-4 or PREP based on fluorescent assay, respectively; SI, selectivity index (calculated as [IC<sub>50</sub> (PREP)/IC<sub>50</sub> (FAP)]). **b**, Autoradioluminographic analysis of the covalent binding of CTR-FAPIs with human serum proteins in vitro. The ligation ratios in per cent are presented beyond corresponding bands. **c**, Autoradioluminographic analysis of the covalent binding of [<sup>177</sup>Lu]Lu-CTR-FAPIs with plasma proteins in mice. **d**, Co-location of the autoradioluminography and Coomassie blue staining results of the human serum incubating with [<sup>177</sup>Lu]Lu-FAPI-mFS up to 12 h. **e**, Renal metabolic

stability of [<sup>177</sup>Lu]Lu-FAPI-mFS in NU/NU mouse by radio-HPLC analysis. Top, the 254 nm UV absorption spectra of <sup>nat</sup>Lu-FAPI-mFS, whose m/z was determined in HPLC-mass spectrometry. Middle, the radio-HPLC spectra of [<sup>177</sup>Lu]Lu-FAPI-mFS before injection. Bottom, the radio-HPLC spectra of urine sample 30 min post-injection of [<sup>177</sup>Lu]Lu-FAPI-mFS. **f**, Radio-HPLC spectra of [<sup>68</sup>Ga]Ga-FAPI-mFS before and after renal metabolism within PET/CT period. **g**, PET/CT images showed for the lesions which [<sup>68</sup>Ga]Ga-FAPI-04 identified, but [<sup>68</sup>Ga]Ga-FAPI-mFS achieved higher tumour uptake. **h**, The reduction in SUV<sub>max</sub> of key organs in patient 1 four hours after injection. Data are representative of two (**b-d**) independent experiments.



**Extended Data Fig. 6 | Further therapeutic data for <sup>177</sup>Lu- or <sup>225</sup>Ac-labelled CTR-FAPIs.** **a–c**, NU/NU mice were implanted subcutaneously with HT-1080-FAP cells, followed by intravenous injection of saline, [<sup>177</sup>Lu]Lu-FAPI-04, [<sup>177</sup>Lu]Lu-FAPI-mFS. n = 7 mice for each group of [<sup>177</sup>Lu]Lu-FAPI-mFS, n = 8 mice for saline and [<sup>177</sup>Lu]Lu-FAPI-04. **a**, Maximum tumour response waterfall plot till Day 30. **b**, Tumour volume curve of an individual mouse. **c**, Photographs of representative tumours at day 14 in a repeated trial. **d–g**, NU/NU mice were implanted subcutaneously with HT-1080-FAP cells, followed by intravenous injection of saline, [<sup>225</sup>Ac]Ac-FAPI-04 or [<sup>225</sup>Ac]Ac-FAPI-mFS. **d**, Treatment

scheme. n = 6 mice for each group of [<sup>225</sup>Ac]Ac-FAPI-mFS 22.2 kBq, n = 7 mice for saline, [<sup>225</sup>Ac]Ac-FAPI-04 and [<sup>225</sup>Ac]Ac-FAPI-mFS 33.3 kBq. **e**, Tumour volume curves of the group. **f**, Maximum tumour response waterfall plot. **g**, Tumour volume curves of an individual mouse. Two-tailed unpaired Student's t-test was applied (**e** on day -15). **h**, Selected results from complete blood count (CBC) and blood biochemistry tests. ALT = Alanine aminotransferase; AST = Aspartate aminotransferase; ALB = Albumin; UREA = Urea in serum; CREA = Serum creatinine. n = 3, data shown are mean  $\pm$  s.d (**e,h**). One-way ANOVA followed by Tukey's multiple comparison test was applied.

Corresponding author(s): Zhibo Liu

Last updated by author(s): Feb 28, 2024

## Reporting Summary

Nature Portfolio wishes to improve the reproducibility of the work that we publish. This form provides structure for consistency and transparency in reporting. For further information on Nature Portfolio policies, see our [Editorial Policies](#) and the [Editorial Policy Checklist](#).

### Statistics

For all statistical analyses, confirm that the following items are present in the figure legend, table legend, main text, or Methods section.

n/a Confirmed

- The exact sample size ( $n$ ) for each experimental group/condition, given as a discrete number and unit of measurement
- A statement on whether measurements were taken from distinct samples or whether the same sample was measured repeatedly
- The statistical test(s) used AND whether they are one- or two-sided  
*Only common tests should be described solely by name; describe more complex techniques in the Methods section.*
- A description of all covariates tested
- A description of any assumptions or corrections, such as tests of normality and adjustment for multiple comparisons
- A full description of the statistical parameters including central tendency (e.g. means) or other basic estimates (e.g. regression coefficient) AND variation (e.g. standard deviation) or associated estimates of uncertainty (e.g. confidence intervals)
- For null hypothesis testing, the test statistic (e.g.  $F$ ,  $t$ ,  $r$ ) with confidence intervals, effect sizes, degrees of freedom and  $P$  value noted  
*Give  $P$  values as exact values whenever suitable.*
- For Bayesian analysis, information on the choice of priors and Markov chain Monte Carlo settings
- For hierarchical and complex designs, identification of the appropriate level for tests and full reporting of outcomes
- Estimates of effect sizes (e.g. Cohen's  $d$ , Pearson's  $r$ ), indicating how they were calculated

*Our web collection on [statistics for biologists](#) contains articles on many of the points above.*

### Software and code

Policy information about [availability of computer code](#)

Data collection	Nuclear magnetic resonance (NMR) spectra were recorded on Bruker AVANCE 400 MHz spectrometer. The autoradioluminography was performed at Typhoon FLA 9500. High-performance liquid chromatography (HPLC) was performed on a Waters with a Waters PDA eλ Detector. Ultra-performance liquid chromatography-mass spectrometry (UPLC-MS) was performed on an ACQUITY UPLC H-Class PLUS instrument equipped with a Waters PDA eλ Detector and a Waters Acquity QDA mass spectrometer. High-resolution mass spectroscopy was performed on a Bruker Fourier Transform Ion Cyclotron Resonance Mass Spectrometer. The tandem mass samples were analysed on a Thermo Scientific Q Exactive Orbitrap mass spectrometer in conjunction with an Easy-nLC II HPLC (ThermoFisher). The Surface plasmon resonance (SPR) studies were performed on Biacore 8K (cytiva). Confocal fluorescence images were recorded on an A1R-si Laser Scanning Confocal Microscope (Nikon). The radioactivity of samples from in-cell and in vivo was detected by an automatic gamma counter (2480, PerkinElmer). The radiochemical purity of labelled compounds was evaluated using radio-high performance liquid chromatography (radio-HPLC, Eckert&Ziegler) or using a radio-TLC system (Eckert&Ziegler). PET images were taken on microPET (Mediso Medical Imaging Systems) for mice or on tota-body PET/CT scanner (uEXPLORER, United Imaging Health Care) for human. SPECT images were taken on microSPECT (Novel Medical) for mice.
Data analysis	Graphpad Prism 8 was used for statistical analysis. MestReNova 7 was used for NMR analysis. Nikon image software (version 4.0) was used to measure the fluorescence intensity. Nucline NanoScan software (InterViewTM FUSION, Mediso Medical Imaging Systems) was used to determine the radioactivity concentration. Tandem mass spectrometry raw data was searched by pFind 3 to identify the covalent modifications. The residue analysis, molecule docking, and interaction analysis were performed with Molecular Operating Environment (MOE, Canada), GOLD (CCDC, UK) and Discovery Studio Visualizer (BIOVIA), respectively. The molecular dynamics (MD) was performed with Assisted Model Building with Energy Refinement (AMBER 20).

For manuscripts utilizing custom algorithms or software that are central to the research but not yet described in published literature, software must be made available to editors and reviewers. We strongly encourage code deposition in a community repository (e.g. GitHub). See the Nature Portfolio [guidelines for submitting code & software](#) for further information.

## Data

Policy information about [availability of data](#)

All manuscripts must include a [data availability statement](#). This statement should provide the following information, where applicable:

- Accession codes, unique identifiers, or web links for publicly available datasets
- A description of any restrictions on data availability
- For clinical datasets or third party data, please ensure that the statement adheres to our [policy](#)

All data supporting the findings of this study are included in the Article and its Supplementary Information. Source Data for Figures 1–5 and Extended Data Figures 1–5 are available with the paper.

## Research involving human participants, their data, or biological material

Policy information about studies with [human participants or human data](#). See also policy information about [sex, gender \(identity/presentation\), and sexual orientation](#) and [race, ethnicity and racism](#).

Reporting on sex and gender There are two participants in this report, who were determined as male by self-reporting.

Reporting on race, ethnicity, or other socially relevant groupings Race-Asian.

Population characteristics This work contains two cases as a pilot study and there is no population characteristics.

Recruitment The study investigators of Peking University Cancer Hospital & Institute identified and recruited participants according to the study eligibility.

Ethics oversight The clinical investigator-initiated trial (IIT) was approved by the Ethics Review Committee of Peking University Cancer Hospital & Institute (Lot No.2023YJZ20).

Note that full information on the approval of the study protocol must also be provided in the manuscript.

## Field-specific reporting

Please select the one below that is the best fit for your research. If you are not sure, read the appropriate sections before making your selection.

Life sciences  Behavioural & social sciences  Ecological, evolutionary & environmental sciences

For a reference copy of the document with all sections, see [nature.com/documents/nr-reporting-summary-flat.pdf](https://nature.com/documents/nr-reporting-summary-flat.pdf)

## Life sciences study design

All studies must disclose on these points even when the disclosure is negative.

Sample size No statistical methods were used to predetermine the sample sizes. It is impossible to predict the magnitude of experimental variation between animals based on our current knowledge. The group sizes (at least four animals per treatment group) represents the minimum number animals needed to reach statistical significance ( $p < 0.05$ ) between experimental groups.

Data exclusions There were no data exclusions.

Replication All attempts at replication are successful. Experiments results were robust and reproducible. The difference between the treated group and control group were statistically significant in the repetitive experiments.

Randomization No randomization was used in this study. For all in vivo experiments, animals were randomly assigned into a treatment group after tumour inoculation. The starting tumour burden in the treatment and control groups was similar before treatment.

Blinding No blinding was done in this study. Most of the studies contained multiple steps (including the material preparation, mouse tumour treatment, and so on) and the scientists must keep careful track of conditions. It would be exceedingly difficult to blind such studies.

## Behavioural & social sciences study design

All studies must disclose on these points even when the disclosure is negative.

Study description Briefly describe the study type including whether data are quantitative, qualitative, or mixed-methods (e.g. qualitative cross-sectional, quantitative experimental, mixed-methods case study).

Research sample	State the research sample (e.g. Harvard university undergraduates, villagers in rural India) and provide relevant demographic information (e.g. age, sex) and indicate whether the sample is representative. Provide a rationale for the study sample chosen. For studies involving existing datasets, please describe the dataset and source.
Sampling strategy	Describe the sampling procedure (e.g. random, snowball, stratified, convenience). Describe the statistical methods that were used to predetermine sample size OR if no sample-size calculation was performed, describe how sample sizes were chosen and provide a rationale for why these sample sizes are sufficient. For qualitative data, please indicate whether data saturation was considered, and what criteria were used to decide that no further sampling was needed.
Data collection	Provide details about the data collection procedure, including the instruments or devices used to record the data (e.g. pen and paper, computer, eye tracker, video or audio equipment) whether anyone was present besides the participant(s) and the researcher, and whether the researcher was blind to experimental condition and/or the study hypothesis during data collection.
Timing	Indicate the start and stop dates of data collection. If there is a gap between collection periods, state the dates for each sample cohort.
Data exclusions	If no data were excluded from the analyses, state so OR if data were excluded, provide the exact number of exclusions and the rationale behind them, indicating whether exclusion criteria were pre-established.
Non-participation	State how many participants dropped out/declined participation and the reason(s) given OR provide response rate OR state that no participants dropped out/declined participation.
Randomization	If participants were not allocated into experimental groups, state so OR describe how participants were allocated to groups, and if allocation was not random, describe how covariates were controlled.

## Ecological, evolutionary & environmental sciences study design

All studies must disclose on these points even when the disclosure is negative.

Study description	Briefly describe the study. For quantitative data include treatment factors and interactions, design structure (e.g. factorial, nested, hierarchical), nature and number of experimental units and replicates.
Research sample	Describe the research sample (e.g. a group of tagged <i>Passer domesticus</i> , all <i>Stenocereus thurberi</i> within Organ Pipe Cactus National Monument), and provide a rationale for the sample choice. When relevant, describe the organism taxa, source, sex, age range and any manipulations. State what population the sample is meant to represent when applicable. For studies involving existing datasets, describe the data and its source.
Sampling strategy	Note the sampling procedure. Describe the statistical methods that were used to predetermine sample size OR if no sample-size calculation was performed, describe how sample sizes were chosen and provide a rationale for why these sample sizes are sufficient.
Data collection	Describe the data collection procedure, including who recorded the data and how.
Timing and spatial scale	Indicate the start and stop dates of data collection, noting the frequency and periodicity of sampling and providing a rationale for these choices. If there is a gap between collection periods, state the dates for each sample cohort. Specify the spatial scale from which the data are taken.
Data exclusions	If no data were excluded from the analyses, state so OR if data were excluded, describe the exclusions and the rationale behind them, indicating whether exclusion criteria were pre-established.
Reproducibility	Describe the measures taken to verify the reproducibility of experimental findings. For each experiment, note whether any attempts to repeat the experiment failed OR state that all attempts to repeat the experiment were successful.
Randomization	Describe how samples/organisms/participants were allocated into groups. If allocation was not random, describe how covariates were controlled. If this is not relevant to your study, explain why.
Blinding	Describe the extent of blinding used during data acquisition and analysis. If blinding was not possible, describe why OR explain why blinding was not relevant to your study.

Did the study involve field work?  Yes  No

## Field work, collection and transport

Field conditions	Describe the study conditions for field work, providing relevant parameters (e.g. temperature, rainfall).
Location	State the location of the sampling or experiment, providing relevant parameters (e.g. latitude and longitude, elevation, water depth).
Access & import/export	Describe the efforts you have made to access habitats and to collect and import/export your samples in a responsible manner and in

## Access &amp; import/export

compliance with local, national and international laws, noting any permits that were obtained (give the name of the issuing authority, the date of issue, and any identifying information).

## Disturbance

Describe any disturbance caused by the study and how it was minimized.

## Reporting for specific materials, systems and methods

We require information from authors about some types of materials, experimental systems and methods used in many studies. Here, indicate whether each material, system or method listed is relevant to your study. If you are not sure if a list item applies to your research, read the appropriate section before selecting a response.

### Materials & experimental systems

- |                                     |   |
|-------------------------------------|---|
| n/a                                 | Involved in the study   |
| <input type="checkbox"/>            | <input checked="" type="checkbox"/> Antibodies                    |
| <input type="checkbox"/>            | <input checked="" type="checkbox"/> Eukaryotic cell lines         |
| <input checked="" type="checkbox"/> | <input checked="" type="checkbox"/> Palaeontology and archaeology |
| <input type="checkbox"/>            | <input checked="" type="checkbox"/> Animals and other organisms   |
| <input type="checkbox"/>            | <input checked="" type="checkbox"/> Clinical data                 |
| <input checked="" type="checkbox"/> | <input checked="" type="checkbox"/> Dual use research of concern  |
| <input checked="" type="checkbox"/> | <input checked="" type="checkbox"/> Plants                        |

### Methods

- |                                     |   |
|-------------------------------------|---|
| n/a                                 | Involved in the study                           |
| <input checked="" type="checkbox"/> | <input type="checkbox"/> ChIP-seq               |
| <input checked="" type="checkbox"/> | <input type="checkbox"/> Flow cytometry         |
| <input checked="" type="checkbox"/> | <input type="checkbox"/> MRI-based neuroimaging |

## Antibodies

## Antibodies used

Anti-FAP: IHC-P, Abcam, ab314456, RM1080, 1:50; Anti-Calcitonin: IHC-P, Abcam, ab133235, EPR68(2), 1:100; Anti-Synaptophysin: IHC-P, Abcam, ab32127, YE269, 1:100; Anti-CEA: IHC-P, Abcam, ab207718, EPR20721, 1:100; Anti-Cga: IHC-P, Abcam, ab283265, RM1025, 1:100; Anti-AE1/AE3: IHC-P, Abcam, ab7753, C-11, 1:100; Anti-Cytokeratin 5/6: IHC-P, Abcam, ab20, LP34, 1:100; Anti-Cytokeratin 7: IHC-P, Abcam, ab183344, SP52, 1:100.

## Validation

All antibodies are validated to be suitable for the corresponding application according to the statements on manufacturer's website.

## Eukaryotic cell lines

Policy information about [cell lines and Sex and Gender in Research](#)

## Cell line source(s)

The human fibrosarcoma HT1080 cell line transfected with FAP (HT-1080-FAP) was purchased from WuXi AppTec, China. The human prostate cancer LNCaP clone FGC cell line (LNCaP) and human prostate cancer 22RV1 cell line (22RV1) were purchased from a local supplier (Procell).

## Authentication

Identity of the cell lines were frequently checked by their morphological features and they were authenticated by the short tandem repeat (STR) profiling initially.

## Mycoplasma contamination

Cells were regularly tested and confirmed without mycoplasma contamination.

Commonly misidentified lines  
(See [ICLAC](#) register)

No commonly misidentified cell lines are used in this study.

## Palaeontology and Archaeology

## Specimen provenance

Provide provenance information for specimens and describe permits that were obtained for the work (including the name of the issuing authority, the date of issue, and any identifying information). Permits should encompass collection and, where applicable, export.

## Specimen deposition

Indicate where the specimens have been deposited to permit free access by other researchers.

## Dating methods

If new dates are provided, describe how they were obtained (e.g. collection, storage, sample pretreatment and measurement), where they were obtained (i.e. lab name), the calibration program and the protocol for quality assurance OR state that no new dates are provided.

Tick this box to confirm that the raw and calibrated dates are available in the paper or in Supplementary Information.

## Ethics oversight

Identify the organization(s) that approved or provided guidance on the study protocol, OR state that no ethical approval or guidance was required and explain why not.

Note that full information on the approval of the study protocol must also be provided in the manuscript.

## Animals and other research organisms

Policy information about [studies involving animals](#); [ARRIVE guidelines](#) recommended for reporting animal research, and [Sex and Gender in Research](#)

Laboratory animals	NU/NU or NOD/SCID mice were used for animal experiments described in this study.
Wild animals	The study did not involve wild animals.
Reporting on sex	The HT-1080-FAP tumour-bearing mice are female. The LNCaP and 22RV1 tumour-bearing mice are male. The STD-PDX model mice are male.
Field-collected samples	The study did not involve samples collected from the field.
Ethics oversight	All animal experiments were performed in accordance with the guidelines approved by the Ethics Committee of Peking University.

Note that full information on the approval of the study protocol must also be provided in the manuscript.

## Clinical data

Policy information about [clinical studies](#)

All manuscripts should comply with the ICMJE [guidelines for publication of clinical research](#) and a completed [CONSORT checklist](#) must be included with all submissions.

Clinical trial registration	NCT06084767.
Study protocol	The full trial protocol can be accessed on the ClinicalTrials.gov website.
Data collection	The patient PET-CT was performed 1-hour post injection in a total-body PET-CT scanner (uEXPLORER, United Imaging Health Care). 3D Slicer software platform (version 4.0, open source) was used to process the data to get the radioactivity biodistribution based on Standard Uptake Value (SUV). The renal metabolic stability of [68Ga]Ga-FAPI-mFS was analysed on radio-HPLC and compared to the quality control spectra.
Outcomes	The conclusion of the registered clinical trial has not been made as it is still undergoing. According to the pilot study, PET-CT imaging of [68Ga]Ga-FAPI-mFS in two patient showed significantly higher tumour uptake than that of [68Ga]Ga-FAPI-04. The radio-HPLC assay of urine sample taken at 30 min post-injection has the same retention time as the original [68Ga]Ga-FAPI-mFS, suggesting that the stability is over 99%.

## Dual use research of concern

Policy information about [dual use research of concern](#)

### Hazards

Could the accidental, deliberate or reckless misuse of agents or technologies generated in the work, or the application of information presented in the manuscript, pose a threat to:

No	Yes
<input checked="" type="checkbox"/>	<input type="checkbox"/> Public health
<input checked="" type="checkbox"/>	<input type="checkbox"/> National security
<input checked="" type="checkbox"/>	<input type="checkbox"/> Crops and/or livestock
<input checked="" type="checkbox"/>	<input type="checkbox"/> Ecosystems
<input checked="" type="checkbox"/>	<input type="checkbox"/> Any other significant area

## Experiments of concern

Does the work involve any of these experiments of concern:

- | No                                  | Yes   |
|-------------------------------------|---|
| <input checked="" type="checkbox"/> | Demonstrate how to render a vaccine ineffective                             |
| <input checked="" type="checkbox"/> | Confer resistance to therapeutically useful antibiotics or antiviral agents |
| <input checked="" type="checkbox"/> | Enhance the virulence of a pathogen or render a nonpathogen virulent        |
| <input checked="" type="checkbox"/> | Increase transmissibility of a pathogen                                     |
| <input checked="" type="checkbox"/> | Alter the host range of a pathogen  |
| <input checked="" type="checkbox"/> | Enable evasion of diagnostic/detection modalities                           |
| <input checked="" type="checkbox"/> | Enable the weaponization of a biological agent or toxin                     |
| <input checked="" type="checkbox"/> | Any other potentially harmful combination of experiments and agents         |

## Plants

### Seed stocks

*Report on the source of all seed stocks or other plant material used. If applicable, state the seed stock centre and catalogue number. If plant specimens were collected from the field, describe the collection location, date and sampling procedures.*

### Novel plant genotypes

*Describe the methods by which all novel plant genotypes were produced. This includes those generated by transgenic approaches, gene editing, chemical/radiation-based mutagenesis and hybridization. For transgenic lines, describe the transformation method, the number of independent lines analyzed and the generation upon which experiments were performed. For gene-edited lines, describe the editor used, the endogenous sequence targeted for editing, the targeting guide RNA sequence (if applicable) and how the editor was applied.*

### Authentication

*Describe any authentication procedures for each seed stock used or novel genotype generated. Describe any experiments used to assess the effect of a mutation and, where applicable, how potential secondary effects (e.g. second site T-DNA insertions, mosaicism, off-target gene editing) were examined.*

## ChIP-seq

### Data deposition

- Confirm that both raw and final processed data have been deposited in a public database such as [GEO](#).
- Confirm that you have deposited or provided access to graph files (e.g. BED files) for the called peaks.

### Data access links

*May remain private before publication.*

*For "Initial submission" or "Revised version" documents, provide reviewer access links. For your "Final submission" document, provide a link to the deposited data.*

### Files in database submission

*Provide a list of all files available in the database submission.*

### Genome browser session (e.g. [UCSC](#))

*Provide a link to an anonymized genome browser session for "Initial submission" and "Revised version" documents only, to enable peer review. Write "no longer applicable" for "Final submission" documents.*

## Methodology

### Replicates

*Describe the experimental replicates, specifying number, type and replicate agreement.*

### Sequencing depth

*Describe the sequencing depth for each experiment, providing the total number of reads, uniquely mapped reads, length of reads and whether they were paired- or single-end.*

### Antibodies

*Describe the antibodies used for the ChIP-seq experiments; as applicable, provide supplier name, catalog number, clone name, and lot number.*

### Peak calling parameters

*Specify the command line program and parameters used for read mapping and peak calling, including the ChIP, control and index files used.*

### Data quality

*Describe the methods used to ensure data quality in full detail, including how many peaks are at FDR 5% and above 5-fold enrichment.*

### Software

*Describe the software used to collect and analyze the ChIP-seq data. For custom code that has been deposited into a community repository, provide accession details.*

# Flow Cytometry

## Plots

Confirm that:

- The axis labels state the marker and fluorochrome used (e.g. CD4-FITC).
- The axis scales are clearly visible. Include numbers along axes only for bottom left plot of group (a 'group' is an analysis of identical markers).
- All plots are contour plots with outliers or pseudocolor plots.
- A numerical value for number of cells or percentage (with statistics) is provided.

## Methodology

### Sample preparation

*Describe the sample preparation, detailing the biological source of the cells and any tissue processing steps used.*

### Instrument

*Identify the instrument used for data collection, specifying make and model number.*

### Software

*Describe the software used to collect and analyze the flow cytometry data. For custom code that has been deposited into a community repository, provide accession details.*

### Cell population abundance

*Describe the abundance of the relevant cell populations within post-sort fractions, providing details on the purity of the samples and how it was determined.*

### Gating strategy

*Describe the gating strategy used for all relevant experiments, specifying the preliminary FSC/SSC gates of the starting cell population, indicating where boundaries between "positive" and "negative" staining cell populations are defined.*

- Tick this box to confirm that a figure exemplifying the gating strategy is provided in the Supplementary Information.

# Magnetic resonance imaging

## Experimental design

### Design type

*Indicate task or resting state; event-related or block design.*

### Design specifications

*Specify the number of blocks, trials or experimental units per session and/or subject, and specify the length of each trial or block (if trials are blocked) and interval between trials.*

### Behavioral performance measures

*State number and/or type of variables recorded (e.g. correct button press, response time) and what statistics were used to establish that the subjects were performing the task as expected (e.g. mean, range, and/or standard deviation across subjects).*

## Acquisition

### Imaging type(s)

*Specify: functional, structural, diffusion, perfusion.*

### Field strength

*Specify in Tesla*

### Sequence & imaging parameters

*Specify the pulse sequence type (gradient echo, spin echo, etc.), imaging type (EPI, spiral, etc.), field of view, matrix size, slice thickness, orientation and TE/TR/flip angle.*

### Area of acquisition

*State whether a whole brain scan was used OR define the area of acquisition, describing how the region was determined.*

### Diffusion MRI

- Used
- Not used

## Preprocessing

### Preprocessing software

*Provide detail on software version and revision number and on specific parameters (model/functions, brain extraction, segmentation, smoothing kernel size, etc.).*

### Normalization

*If data were normalized/standardized, describe the approach(es): specify linear or non-linear and define image types used for transformation OR indicate that data were not normalized and explain rationale for lack of normalization.*

### Normalization template

*Describe the template used for normalization/transformation, specifying subject space or group standardized space (e.g. original Talairach, MNI305, ICBM152) OR indicate that the data were not normalized.*

### Noise and artifact removal

*Describe your procedure(s) for artifact and structured noise removal, specifying motion parameters, tissue signals and physiological signals (heart rate, respiration).*

## Volume censoring

Define your software and/or method and criteria for volume censoring, and state the extent of such censoring.

## Statistical modeling &amp; inference

## Model type and settings

Specify type (mass univariate, multivariate, RSA, predictive, etc.) and describe essential details of the model at the first and second levels (e.g. fixed, random or mixed effects; drift or auto-correlation).

## Effect(s) tested

Define precise effect in terms of the task or stimulus conditions instead of psychological concepts and indicate whether ANOVA or factorial designs were used.

Specify type of analysis:  Whole brain  ROI-based  Both

## Statistic type for inference

Specify voxel-wise or cluster-wise and report all relevant parameters for cluster-wise methods.

(See [Eklund et al. 2016](#))

## Correction

Describe the type of correction and how it is obtained for multiple comparisons (e.g. FWE, FDR, permutation or Monte Carlo).

## Models &amp; analysis

## n/a Involved in the study

- Functional and/or effective connectivity
- Graph analysis
- Multivariate modeling or predictive analysis

## Functional and/or effective connectivity

Report the measures of dependence used and the model details (e.g. Pearson correlation, partial correlation, mutual information).

## Graph analysis

Report the dependent variable and connectivity measure, specifying weighted graph or binarized graph, subject- or group-level, and the global and/or node summaries used (e.g. clustering coefficient, efficiency, etc.).

## Multivariate modeling and predictive analysis

The molecular dynamics (MD) was performed with Assisted Model Building with Energy Refinement (AMBER 20). Four docked complexes, namely Lu-FAPI-pFS:Y210-FAP, Lu-FAPI-pFS:Y450-FAP, Lu-FAPI-mFS:Y210-FAP and Lu-FAPI-mFS:Y450-FAP, with covalent linkages at S624, were selected as the initial structures for MD simulations. The ff19SB force field was employed for the protein, and the TIP3P model was used for solvent water molecules. The force field parameters of ligands were generated from the AM1-BCC force field. The initial coordinates and topology files were generated by the xleap program with neutralization and solvation. All models were treated with the same MD protocols via employing the periodic boundary condition with cubic models. First, minimizations were carried out to relax the solvent and optimize the system. After, each system was heated from 0 to 300 K gradually under the NVT ensemble over 20 ps. Then, another 200 ps MD simulations at 300 K and the target pressure of 1.0 atm were carried out in the NPT ensemble, during which the system temperature was controlled by the Langevin thermostat method. Afterward, a preliminary 150 ns MD simulation under the NVT ensemble at 300 K was performed for each model to assess the propensity of ligation. All hydrogen-containing bonds during the MD simulations were constrained using the SHAKE algorithm. A cut-off of 12 Å was set for van der Waals and no cut-off for electrostatic interactions. The CPPTRAJ module was used to analyse MD trajectory data. The last frame ( $t = 1$  ns) of the trajectory was extracted for pose analysis (Fig. S11). Variation of the distance between the oxygen atom of Y210/Y450 and the sulphur atom of the FS warhead during simulation was monitored (Fig. S13). Lu-FAPI-pFS:Y210-FAP and Lu-FAPI-mFS:Y450-FAP were each subjected to a 10 ns NVT simulation to obtain an equilibrated structure, based on which the FS group and the corresponding tyrosine was then covalently linked. Subsequently, the bonded complexes Lu-FAPI-pFS-Y210-FAP and Lu-FAPI-mFS-Y450-FAP underwent NVT simulations for 50 ns.